energy&fuels

pubs.acs.org/EF
Article

Defect-Engineered High-Entropy Spinel Oxide@Onion-Like Carbon Catalysts for High-Areal-Energy Rechargeable Zinc−Air Batteries

Agnes Mongwe, Aderemi B. Haruna, Lesego Gaolatlhe, Joesene Soto, Zixiao Shi, Patrick V. Mwonga, Xiao-Yu Yang, David A. Muller, Héctor D. Abruña,* and Kenneth I. Ozoemena*

Cite This: *Energy Fuels* 2025, 39, 13105−13119

Read Online

ACCESS | Metrics & More | Article Recommendations | Supporting Information

ABSTRACT: Rechargeable zinc-air batteries (ReZAB) have emerged as the next-generation batteries with several advantages over the conventional lithium-ion battery. In this work, single nanocrystals of inverse-type high-entropy spinel oxides (HESOx, particle size of 10−12 nm) confined in highly curved defective onion-like carbons (HESOx/OLC$_{AT}$) as efficient electrocatalysts for oxygen evolution reaction (OER), oxygen reduction reaction (ORR), and ReZAB, have been synthesized. The HESOx materials were thoroughly characterized using several analytical techniques, including X-ray diffraction (XRD), X-ray photoelectron spectroscopy (XPS), scanning transmission electron microscopy (STEM), Raman, and electron paramagnetic resonance (EPR). HESOx/OLC$_{AT}$ catalyst was tested for ReZAB using literature-recommended parameters that would allow for real technological application. These parameters include a current loading of 10 mA cm^{-2} and a discharge areal energy density of 35 mWh cm$_{geometric}^{-2}$, which maps a Li-ion battery pack-level specific energy of 120 Wh kg$_{pack}^{-1}$. HESOx/OLC$_{AT}$ electrocatalysts allowed for continuous discharging and charging at a current loading of 10 mA cm^{-2} with discharge areal energy densities between 37 and 74 mWh cm$_{geometric}^{-2}$, thus outperforming the recommended threshold of 35 mWh cm$_{geometric}^{-2}$. Considering that most studies (>90%) hardly meet the recommended threshold for technological application of ReZAB, the present work represents one of the top-performing electrocatalysts for ReZAB. The excellent electrocatalytic properties of defect-rich HESOx/OLC$_{AT}$ toward ORR/OER and ReZAB are governed by the strong electronic modulation arising from d-π hybridization, the availability of multiple catalytic sites for intermediates, and weakened d-band centers of the rate-determining intermediates (i.e., *O adsorption for ORR and *OOH formation for OER) compared to the pristine HESOx. This work introduces an effective approach for the design and synthesis of single nanocrystals of high-entropy electrocatalysts for the development of low-cost, robust, and technologically relevant rechargeable zinc−air batteries.

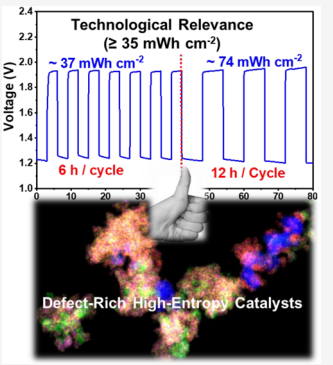

INTRODUCTION

Energy storage is still one of the most important challenges facing the global economy. It is critical if the world must fulfill some of its most urgent sustainable development goals, such as good health and well-being, affordable and clean energy, and mitigation of climate deterioration, to mention only a few. It is generally accepted that battery technologies are a key part of the puzzle when it comes to enabling widespread electric transportation, personal electronics, smart grids/cities, renewable energy, and off-grid electrification. Global commitment to reduce emissions in the transport sector has led to the emergence of new energy vehicles (NEVs) with a smaller carbon footprint. Battery electric vehicles (BEVs) are gaining traction because of their low emission profile.

For more than three decades, lithium-ion batteries (LIBs) have dominated the battery industry. However, aside from being too expensive and unsafe, it has been accepted that LIBs are fast approaching their maximum ability to store and generate electricity. Therefore, there is an urgent need for advanced batteries that can meet the energy demand of the next generation of consumer technologies. Rechargeable zinc-air battery (ReZAB) is a battery technology with a huge potential to meet the Sustainable Development Goal (especially, Goal # 7: Affordable and clean energy) of the United Nations. ReZAB is a safe and environmentally friendly technology. ReZAB can provide a localized energy source for powering electronic devices, electric vehicles, and power reserves while improving access, safety, and reliability. ReZAB represents one of the unique battery technologies, as it uses ordinary air (oxygen), cheap zinc, and alkaline water to store and generate electricity.

ReZAB boasts several advantages over the LIB and other battery technologies,[1−3] and has been gaining traction in recent years.[4−7] For example, (1) it is safe to use (it uses water as an electrolyte, not the flammable organic liquid used in

Received: April 18, 2025
Revised: June 8, 2025
Accepted: June 16, 2025
Published: June 25, 2025

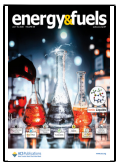

LIB); (2) it is a low-cost technology because of the natural abundance of its critical raw materials (zinc, air, water, and transition metals such as manganese). In general, unlike other battery technologies, such as LIBs, lead-acid batteries, and nickel−metal hydride, ReZAB is environmentally benign and recyclable. Additionally, the abundance of its materials does not constitute the risk of low supply; (3) it possesses high theoretical specific energy density (1086 Wh/kg), which is about five times greater than that of the conventional LIB; (4) the practical specific energy density of ReZAB is the same as that of the Li−air battery (450 wh/kg); and (5) its manufacturing/capital cost (about US$50) is as low as that of the conventional lead-acid battery.

For these compelling reasons, ReZAB can be used in a plethora of applications, such as portable electronics (such as mobile phones and laptops), wearable power electronics, grid electricity storage, home electricity, electric vehicles, and aircraft, to mention a few. Despite the huge advantages of ReZABs, some technical challenges have continued to conspire against their widespread development and commercialization. A key challenge is the sluggish kinetics of the oxygen reduction reaction (ORR) and oxygen evolution reaction (OER). Although carbon-supported noble metal electrocatalysts such as platinum group metals (PGMs) can improve the kinetics of ORR, they are extremely poor for OER.[8,9] The high cost and low electrochemical stability of PGMs make them undesirable for large-scale/practical applications. Thus, there is a continuing need to develop robust and low-cost transition-metal-based bifunctional electrocatalysts that will drive ORR and the OER in ReZABs.

In the past decade, there has been an increased interest in the R&D of ReZAB because of the urgent global demand for a more affordable, safe-to-use, environmentally friendly, and high-energy battery technology that can support the next generation of commercial and renewable energy technologies. There are several scientific papers on ReZABs that have claimed to have made some technological breakthroughs in this battery system. However, in 2020, Rolison group examined these scientific articles, and very disappointingly, found that only 8 out of the 100 articles could claim to have made a real technological breakthrough.[2] According to Rolison and co-workers, a real technological breakthrough in ReZAB can be claimed only if the ReZAB can compete with lithium-ion batteries. According to the authors, "*to compete with Li-ion batteries, researchers should cycle zinc−air cells at 35 mWh* cm^{-2}".[2]

Motivated by the proposed threshold for developing technologically relevant ReZABs, we report on defect-rich single nanocrystals of high-entropy inverse spinel oxides $(CuMnFeNiCo)_3O_4$ on onion-like carbons (OLC) (herein abbreviated as $HESOx/OLC_{AT}$) as a highly efficient bifunctional electrocatalyst for ORR/OER and ReZAB. Corner and edge sites of catalysts have been known to exhibit enhanced electrocatalytic activities. To mimic metal sites at the corners and edges of particles, this work uses highly curved carbon support to anchor HESOx sites. The excellent physicochemical properties of OLC, including high-curvature, small nanoparticles <10 nm, and high electrical conductivity (~4 S cm^{-1}), make it the ultimate candidate for anchoring HESOx. We show that $HEXOx/OLC_{AT}$ complex achieved 74 mWh $cm_{geometric}^{-2}$ (Note that 'geometric' means the geometric surface area of the electrode or current collector) exceeding the threshold of 35 mWh $cm_{geometric}^{-2}$ at a current loading of 10 mA cm^{-2} with excellent 'bifunctionality index' ($\Delta E = |E_{1/2(ORR)} - E_{j=10(OER)}|$) of 0.75 V. The effect of strong electronic modulation arising from d-π hybridization and weakened d-band centers in the $HESOx/OLC_{AT}$ complex that allowed for the superior electrocatalysis for ReZAB are highlighted.

EXPERIMENTAL SECTION

Materials. The reagents used in this study were of analytical grade and were used without further purification. The precursors, $Co(NO_3)_2{\cdot}6H_2O$, $Cu(NO_3)_2{\cdot}3H_2O$, $Fe(NO_3)_3{\cdot}9H_2O$, $Mn(NO_3)_2{\cdot}4H_2O$, $Ni(NO_3)_2{\cdot}6H_2O$, ethylene glycol, and citric acid were purchased from Sigma-Aldrich. The onion-like carbon (OLC) was obtained by annealing denoted nanodiamonds (98−99% purity, NaBond Technologies Co.) at a temperature of 1300 °C as described in ref 3. Commercial Pt/C (10 wt %) and IrO_2 (99.9%) were also obtained from Sigma-Aldrich.

Synthesis of Single Nanocrystals of High-Entropy Inverse Spinel Oxides $(CoCuFeMnNi)_3O_4$ (HESOx). The high-entropy spinel oxides were synthesized using a one-step powder-forming Pechini method,[10] exemplified in Figure S1. Briefly, stoichiometric amounts of the metal nitrate salts were prepared, where each metal nitrate salt was dissolved in deionized water and magnetically stirred to obtain adequate homogeneity. Citric acid was dissolved in deionized water, and this was followed by the addition of ethylene glycol to obtain the CA-EG mixture (1:4). The metal nitrate solutions were mixed and added dropwise into the CA-EG mixture and left to stir while heating at 90 °C. The metal nitrate solution eventually dehydrated into a gel but was kept at 90 °C until the gel burned, ultimately forming a porous black metal oxide powder. The powder was subsequently calcined at 500 °C for 6 h in air to obtain a black powder and subsequently annealed at 550 °C for 6 h under inert argon atmosphere to obtain a black crystalline powder (designated herein as **HESOx**).

Loading HESOx onto Onion-like Carbon (OLC). The loading of HESOx onto the OLC is summarized as shown in Figure S2. Briefly, 360 mg of OLC was first stirred in 20 mL of ethylene glycol in a 3-neck flask. Into this, "solution A" (containing 4 mL of water, 4 mL of ethylene glycol, 0.5 mL of HCl (32%), and 40 mg of HESOx) was added dropwise. A separate mixture of NaOH (0.40 g) in H_2O (0.80 mL) mixed in EG (2.8 mL) was prepared ("Solution B") and added to the mixture. The reaction mixture was heated at 125 °C for 3 h under a nitrogen atmosphere. After cooling to room temperature, the solid products were washed with distilled water until the filtrate pH became neutral. The final product was then dried at 40 °C in a vacuum oven (designated as $\mathbf{HESOx/OLC_{AT}}$, where "AT" signifies acid/alkaline treatment). The synthesis of **HESOx/OLC** follows the same procedure, except that HCl and NaOH were omitted in the sample preparation. The stoichiometry of the metal composition was established using inductively coupled plasma atomic emission spectroscopy (ICP-AES) at the Cornell Nutrient Analysis Laboratory (CNAL) using conventional digestion with aqua regia (HNO_3/HCl 1:4 v/v).

Physical Characterization. The scanning transmission electron microscopy (STEM) experiment was performed using Thermo Fisher FEI Spectra 300 TEM with ultrahigh-brightness cold field emission gun (C-FEG) and spherical aberration correction (aka. "Kraken" at Cornell University). The STEM resolution is 58 pm with probe current = 75 pA. The high-annular angle dark-field (HAADF) image was collected with C2 aperture = 70 μm, camera length = 94 mm, and convergence angle = 30 mrad with 60 mrad inner and 200 mrad out collection angles. The HAADF image stacks were taken with 2048 × 2048 pixels with 200 ns dwell times to 30 frames, and then the image stacks were summed to one frame after rigid registration to enhance signal-to-noise ratio (SNR) and reduce the effect of sample drift. The energy-dispersive X-ray spectroscopy (EDS) experiment was performed using a Super-X EDS detector with probe current = 600 pA.

XRD characterizations were performed on a Bruker D2 phaser. The Zeiss Auriga Field emission scanning microscopy (SEM) powered by

https://doi.org/10.1021/acs.energyfuels.5c02012
Energy Fuels 2025, 39, 13105−13119

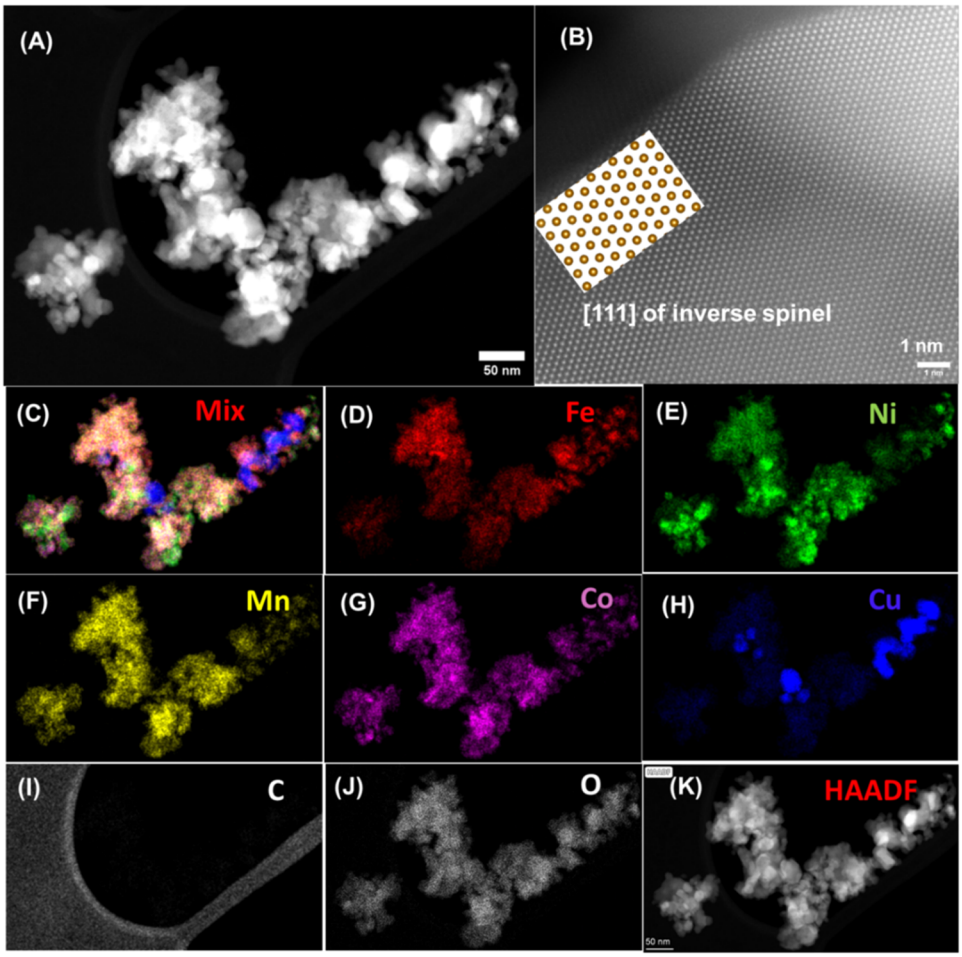

Figure 1. STEM HAADF images of a typical HESOx/OLC$_{AT}$: (A) Particle STEM image of HESOx/OLC$_{AT}$; (B) STEM-HAADF image of HESOx/OLC$_{AT}$ particle, (C–J) STEM EDX maps of individual elements and (K) HAADF of the particle.

SmartSEM was used to obtain SEM images, and the Oxford X-max with Aztech software was used to obtain EDX data. Thermogravimetric analyses (TGA) of the samples were carried out using a TGA 4000 Perkin Elmer at a heating rate of 10 °C/min, under air (20 mL/min) from 35 to 900 °C. The surface structure of the catalysts was examined using a Thermo Fisher Scientific Nexsa G2 Surface analysis system, which was equipped with an aluminum Kα source (1486.68 eV) from the Cornell Center for Materials Research (CCMR) at Cornell University. A spot size of 400 μm was selected for all of the measurements. The survey spectrum was recorded with a resolution/pass energy of 200 eV and an energy step size of 1 eV. The elemental regions were recorded with a resolution/pass energy of 50 eV and a step size of 0.1 eV to obtain better resolution. All of the samples were measured in powder form using copper tape as the loading template.

Electrochemical Testing (Half-Cell Measurements). The electrochemical measurements were carried out at room temperature using the Biologic VSP300 potentiostat powered by EC lab or Pine Research Instrumentation WaveDriver 200 potentiostat with a rotating disk electrode (RDE) setup. Briefly, for the HESOx, HESOx/OLC, and HESOx/OLC$_{AT}$, each sample was dispersed in pure ethanol (1 mL) containing 5% Nafion (50 uL) and sonicated in ice-cold water for 1 h. Carbon rod or Pt rod was used as the counter electrode, while AglAgCl (3 M KCl) was used as the reference electrode. Oxygen-saturated 1 M KOH was used as the electrolyte for both the ORR and the OER. Linear sweep voltammograms (LSV) were conducted at a scan rate of 10 mV/s. The area of the electrode or current collector in this work is geometric rather than gravimetric or an electroactive surface area. The electrochemical impedance spectroscopy (EIS) was performed at a frequency range of 100 kHz to 0.01 Hz and $E_{j=10}$ potential for different materials.

Rotating ring and disk electrode (RRDE) experiments were conducted with an electrode consisting of a glassy carbon disk and gold ring. The ORR activity was tested by using CV with an RRDE setup. Background measurements were run first, starting at 1.1 V and finishing at 0.4 V vs RHE at a scan rate of 5 mV s^{-1} and 1600 rpm in an Ar-saturated 1 M KOH. For the ORR measurements, an additional CV was acquired at the same potential window, scan rate, and rpm while under oxygen-saturated 1 M KOH solution. The RRDE experiments were done by selecting a bias of 1.2 V versus RHE at the ring in collection efficiency mode to acquire the current associated with peroxide formation.

Using the geometrical area of the electrode, the current density was normalized and the potentials were converted to a reversible hydrogen electrode (RHE) using the following Nernst equation

$$E_{RHE} = E_{Ag/AgCl} + 0.059 \times pH + 0.1976 \quad (1)$$

To calculate the overpotential (η) for the OER, the following formula was used

$$\eta\ (V) = E_{RHE} - 1.23 \quad (2)$$

For the ORR, analysis was done using CV data taken at 2025, 1600, 1225, 900, 625, and 400 rpm. The limiting current values at 0.5 V of all of the CVs were used and the number of electrons transferred (n) from the RDE experiments was calculated using the Koutecký–Levich (KL) equation

$$\frac{1}{j} = \frac{1}{j_k} + \left(\frac{1}{0.62nFAD_o^{2/3}\vartheta^{-1/6}C_o}\right)\omega^{-1/2} \quad (3)$$

https://doi.org/10.1021/acs.energyfuels.5c02012
Energy Fuels 2025, 39, 13105–13119

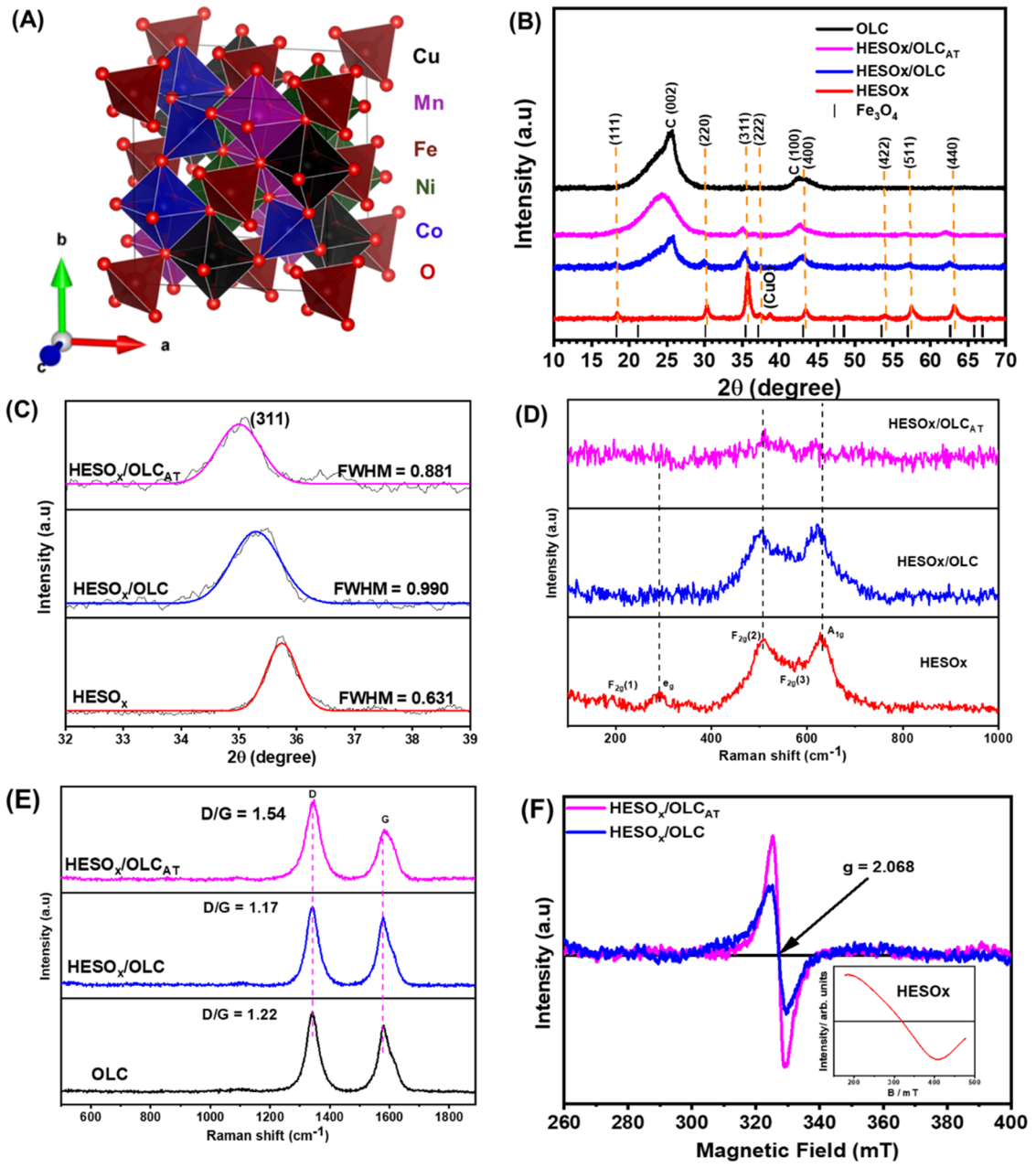

Figure 2. (A) Schematic crystal structure of the HESOx material studied in this work uses Fe_3O_4 as a parent spinel structure. The powder XRD patterns of (B) HESOx, HESOx/OLC, HESOx/OLC$_{AT}$, and OLC modeled with the Bragg lines of the parent Fe_3O_4 inverse spinel oxide. (C) Zoomed-in (311) plane for HESOx, HESOx/OLC, and HESOx/OLC$_{AT}$. Raman spectra taken at the expected regions for the (D) spinel oxide and (E) carbon. (F) EPR spectra of HESOx/OLC and HESOx/OLC$_{AT}$, with the inset showing the EPR of the pristine HESOx.

where j is the current density, j_k is the kinetic current density, F is the Faraday constant (96 485.3321 C mol^{-1}), A is the geometric area of the electrode, D_o is the diffusion coefficient of oxygen (1.93×10^{-5} cm^2 s^{-1}), υ is the viscosity of the solution (1.009×10^{-2} cm^2 s^{-1}), C_o is the concentration of oxygen dissolved in solution (0.78×10^{-6} mol cm^{-3}), and ω is the rotation speed in rpm.

H_2O_2 selectivity and electron transfer numbers (n) were calculated from the RRDE experiments using the following equations

$$\text{H}_2\text{O}_2 \text{ selectivity: } \%\text{H}_2\text{O}^- = 200\left(\frac{\frac{I_{ring}}{N}}{I_{disk} + \frac{I_{ring}}{N}}\right) \quad (4)$$

$$\text{electron transfer number: } n = 4\left(\frac{4I_{disk}}{I_{disk} + \frac{I_{ring}}{N}}\right) \quad (5)$$

where the polarization curves were used to calculate the Tafel slopes.

$$\eta = b(\log j) + a \quad (6)$$

where b is the Tafel slope and j is the disk current.

Fabrication and Testing of Rechargeable Zinc–Air Battery (ReZAB) Cells. A homemade cell was fabricated to measure the performance of the catalysts in rechargeable zinc–air batteries. A zinc plate with a thickness of 0.25 mm was used as the anode, and the gas diffusion layer (carbon paper) coated with the catalyst was used as the air cathode. The carbon paper with a geometric area of 1 cm^2 was

https://doi.org/10.1021/acs.energyfuels.5c02012
Energy Fuels 2025, 39, 13105−13119

used, and 10 mg of the catalyst was loaded on the paper. A conventional electrolyte (0.2 M zinc acetate dissolved in 6 M KOH) was used. To prepare the catalyst slurry, 10 mg of HESOx/OLC or HESOx/OLC_{AT} was dissolved in 20 μL of water, 180 μL of isopropyl alcohol, and 20 μL of PTFE and stirred on a magnetic stirrer. The coated catalyst was oven-dried at 80 °C for 30 min. A rechargeable zinc−air battery with a mixture of Pt/C and IrO_2 (mass ratio of 1:1) was assembled in the same way for comparison. The biologic VSP300 potentiostat was used to collect the reported data on rechargeable zinc−air batteries. The long-term stability was first conducted under shallow cycling conditions at 2 mA cm^{-2} with 30 min discharge and 30 min charge (1 h per cycle). The catalyst was then subjected to harsh cycling conditions (6 and then 12 h per cycle) to meet the minimum required depth of discharge.

RESULTS AND DISCUSSION

Physical Characteristics. ICP-AES analysis (Supporting Information) was used to estimate the stoichiometry of the HESOx/OLC_{AT} as $(Cu_{0.17}Mn_{0.18}Fe_{0.18}Ni_{0.23}Co_{0.24})_3O_4$, which is approximately the expected 0.6 per metallic ion. Figure S3 compares the transmission electron microscope (TEM) images of pristine HESOx, HESOx/OLC, and HESOx/OLC_{AT} at 50 nm resolution. The pristine HESOx comprises single nanocrystals (4−25 nm range) with an average size of ca. 12 nm. As should be expected, it was difficult to observe the HESOx particles when confined in the OLC because of the high carbon content of the crystalline OLC (~90%), as shown by the TGA data (Figure S4). The lattice fringe spacings of the HESOx (Figure S5) were measured as 0.25, 0.29, and 0.47 nm, which correspond to the interplanar spacing of (311), (220), and (111) planes of a spinel crystalline structure, respectively. For HESOx/OLC (Figure S6), an interlayer spacing of 0.337 nm was observed, which corresponds to the graphene (002) plane. TGA results show that thermal stability decreases as HESOx≫ OLC > HESOx/OLC > HESOx/OLC_{AT}, confirming the successful integration of the HESOx with OLC and the subsequent conversion of the pristine HESOx/OLC to the HESOx/OLC_{AT}.

Figure 1A shows a scanning transmission electron microscope (STEM) high-angle annular dark-field (HAADF) image (Figure 1B) of the HESOx/OLC_{AT} showing the image along the [111] axis of the inverse spinel. Except for Cu, all the other elements (Fe, Ni, Co, and Ni) are relatively uniformly distributed in the solid solution. The inability of Cu to fully become part of the solid solution could be due to Jahn−Teller effect, whereby the oxygen sublattice around the Cu ion is locally deformed, making it difficult for CuO to diffuse into the spinel phase.[11]

The schematic crystal structure of the HESOx material is shown in Figure 2A, while Figure 2B represents the powder X-ray diffraction patterns of HESOx studied in this work. The diffraction peaks appear at 18.4, 30.4, 35.7, 37.4, 43.5, 53.9, 57.6, and 62.5° correspond to the (111), (220), (311), (222), (400), (422), (511), and (440) Miller indices, respectively. These diffraction peaks are typical of the conventional inverse spinel oxides. The dominance of the (311) peak in the XRD pattern is a clear indication that these materials assume the crystal structure of an inverse spinel such as Fe_3O_4 or $NiFe_2O_4$. The distinct peak at 38.8° is related to CuO. It is suspected that the Jahn−Teller effect could have led to the isolation of Cu, whereby the oxygen sublattice around the Cu ion is locally deformed, making it difficult for CuO to diffuse into the spinel phase.[11] Since there is no existing crystallographic information file (.cif) for the HESOx in the literature, we obtained one by using naturally occurring Fe_3O_4 as the parent inverse spinel structure. As seen in Figure 2B, the Bragg lines essentially matched the conventional Fe_3O_4 inverse spinel structure; the slight differences should be expected as HESOx (unlike the Fe_3O_4 that contains just one metal) contains five different transition metals with different atomic radii that can lead to distortion in the crystal lattice. Zooming in on the (311) plane (Figure 2C), one can observe a downward shift of 2θ degrees of 35.72, 35.31, and 35.00° for HESOx, HESOx/OLC, and HESOx/OLC_{AT}, respectively, indicating the largest lattice expansion for HESOx/OLC_{AT}. Similarly, the carbon plane (002) showed the highest lattice expansion for HESOx/OLC_{AT} (2θ = 24.24 °) compared to 25.60 ° for both HESOx and HESOx/OLC. The result suggests that the mild acid treatment increases the lattice of HESOx/OLC, which is advantageous for improved ionic transport.

Figure 2D compares the Raman spectra of the various HESOx materials in the band regions between 100 and 1000 cm^{-1}. The bands around 200, 300, 500, 600, and 700 cm^{-1} are characteristic Raman active modes of spinel metal oxides and are related to F_{2g}, E_g, F_{2g}, E_{2g}, and A_{1g}, respectively. The symmetric stretching mode (A_{1g}) is characteristic of the spinel oxide structure (M−O), which is due to the vibration of the octahedral M−O bond. F_{2g} is the symmetric bending mode associated with the vibration of the tetrahedral sites, while E_g is the symmetric deformation mode due to the octahedral sites.

The Raman bands, notably A_{1g}, shifted to a lower region, i.e., from HESOx (631 cm^{-1}) to HESOx/OLC (624 cm^{-1}) and HESOx/OLC_{AT} (614 cm^{-1}). The downward shift is indicative of an increased concentration of oxygen defects, which has been linked to enhanced catalytic activity.[12] Of particular interest is that HESOx/OLC_{AT} shows the weakest intensity of bands, which may be attributed to increased defects. The increase in oxygen defects may be related to the higher surface area of HESOx/OLC_{AT} particles stabilized in nanopockets within the OLC matrix. In other words, HESOx/OLC_{AT} is more defective than its HESOx/OLC and HESOx counterparts. The G band relates to the sp2 hybridized carbon atoms (i.e., graphitic structure) while the D band is due to the high concentration of sp3 hybridized carbon atoms (i.e., defective graphitic structure). The ratio of the area under the D and G bands (i.e., I_D/I_G, Figure 2E) decreased as HESOx/OLC_{AT} (1.54) > OLC (1.22) > HESOx/OLC (1.17), meaning that HESOx/OLC_{AT} is more defective than OLC and HESOx/OLC. The increased sp^3 hybridized carbon is an indication of strong metal oxide-support interactions, such as covalent bonds between the metal oxide and support, improving stability and charge transfer between the HESOx and carbon.[13] Electron paramagnetic resonance (EPR) spectroscopy provides a direct measure of the concentration of the paramagnetic species in the sample. O^- is of particular interest as an indicator of the surface defect concentration, generally grouped as oxygen vacancies in the literature.[14,15] Figure 2F shows the typical room-temperature EPR spectra of HESOx/OLC and HESOx/OLC_{AT}. EPR was used to further interrogate the presence of oxygen vacancies. While the OLC-based HESOx composites showed strong EPR signals (Figure 2F), the pristine materials did not show any useful signal (not shown here), indicating that OLC-based HESOx composites possess high concentrations of unpaired electron contents, arising from the electronic interactions between the OLC and HESOx materials. The EPR signals at g = 2.068 are associated with the electron capture on the oxygen vacancies, with HESOx/

https://doi.org/10.1021/acs.energyfuels.5c02012
Energy Fuels 2025, 39, 13105−13119

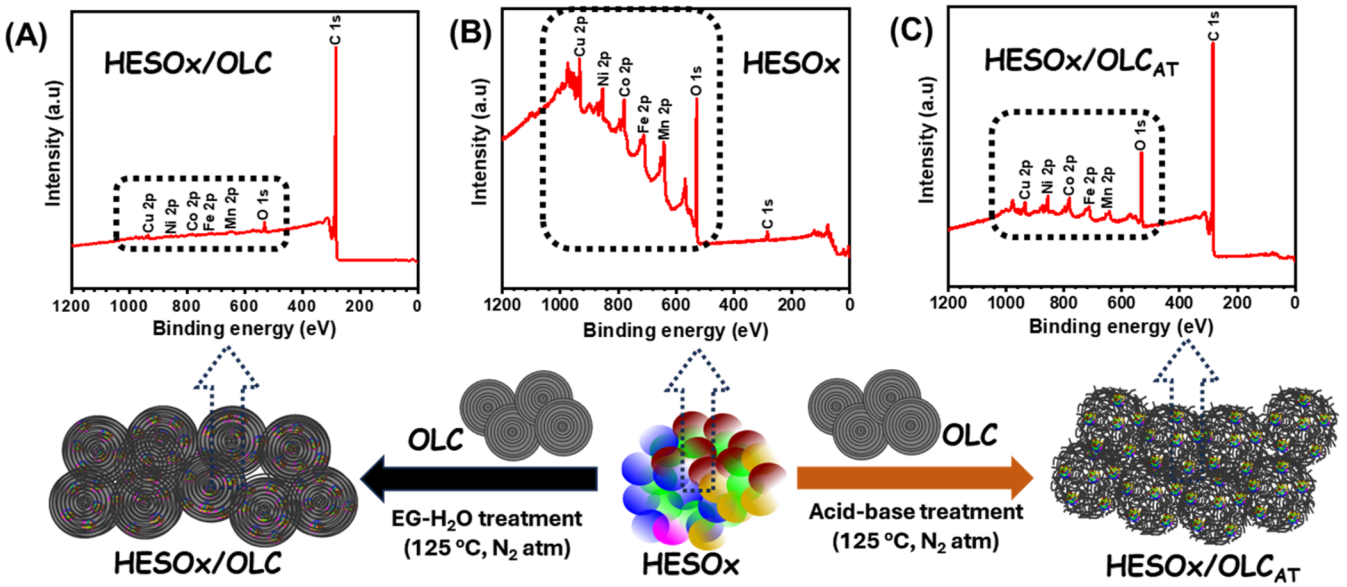

Figure 3. High-resolution XPS survey scan for (A) HESOx/OLC, (B) HESOx, and (C) HESOx/OLC$_{AT}$ with a corresponding carton depiction of the two key products (HESOx and HESOx/OLC$_{AT}$) from their synthesis protocols. Note the protrusion of the surface of HESOx out of the defective OLC, confirmed by the XPS survey scan.

OLC$_{AT}$ exhibiting a stronger peak intensity (i.e., more oxygen vacancies) than HESOx/OLC. The EPR finding corroborates the Raman data. It is well established that defect engineering (oxygen vacancies) provides a unique opportunity to modulate the electronic properties of metal oxides for improved electrocatalytic activities. As would be shown later, HESOx/OLC$_{AT}$ with the highest content of oxygen vacancies gives the best electrocatalytic activities for RZAB. This should perhaps not be surprising, since it is known that oxygen vacancies increase in amorphous oxide materials,[16,17] and boost electrocatalytic response because of the absence of well-defined crystal planes.

Figure 3 depicts the high-resolution XPS survey scans of the pristine HESOx and its products upon subjection to EG-water treatment to give HESOx/OLC and acid−base treatment for defect-rich HESOx/OLC$_{AT}$. The full XPS spectra confirm the presence of elements Cu, Mn, Fe, Ni, Co, and O, in agreement with the EDS results. It is interesting to observe that the XPS survey scan (repeated in both laboratories in the US and SA) shows excellent consistency, whereby surface OLC dominates the HESOx (Figure 3A), while mild acid treatment leads to defective HESOx protruding out of the high-curvature and defective OLC surface (Figure 3C). This protrusion may be related to a type of "tip effect", which is known to enhance electrocatalysis by creating in situ strong local electric field around the catalytic metal site.[13,18]

Next, the XPS spectra of each element in the HESOx were studied to understand the chemical states and structures of the prepared HESOx samples. All of the spectra were successfully fitted using Gaussian−Lorentzian functions after the Shirley background subtraction. Figure 4 represents the deconvoluted high-resolution spectra of Mn 2p (Figure 4A), Fe 2p (Figure 4B), Ni 2p (Figure 4C), Co 2p (Figure 4D), Cu 2p (Figure 4E), and O 1s (Figure 4F) in the pristine and OLC-based HESOx complexes. Each of the M 2p was deconvoluted into two spin−orbit doublets combined with two visible shakeup satellite peaks (abbreviated as "sat" in the figure). For each of the metals (Mn 2p (~641.9 eV), Fe 2p (~711.8 eV), Ni 2p (~854.3 eV), Co 2p (~779.8 eV), and Cu 2p (~933 eV)), the HESOx/OLC$_{AT}$ exhibited the most positive shifts of the deconvoluted M^{2+} and M^{3+} peaks compared to the HESOx/OLC and pristine HESOx complexes, which confirms electron transfer from the metallic elements to the highly curved and defective OLC surface. Importantly, such positive shifts indicate weak d-band centers (especially for the HESOx/OLC$_{AT}$ catalyst) that bode well for enhanced ORR and OER catalysis.[19] For Cu 2p (~ 933 eV), the pristine HESOx exhibited metallic Cu^{o} (930.371 eV) in addition to Cu^{+} (932.991 eV) and Cu^{2+} (934.813 eV). The OLC-based HESOx complexes only showed the Cu^{+} and Cu^{2+}, with very minor positive shifts (~0.2 eV), which indicates that Cu does not significantly contribute to the electron transfer processes in the HESOx complexes.

The O 1s deconvoluted XPS is shown in Figure 4F. Upon introduction of the OLC to the HESOx, the peak shifted to a higher binding energy: pristine HESOx (529.6 eV) < HESOx/OLC ≈ HESOx/OLC$_{AT}$ (531.7 eV). This oxidative shift further confirms the electronic interaction between the OLC and HESOx species. Such electronic modulation of the HESOx by the highly curved OLC should lead to improved electrocatalysis.[20,21] Each of the spectra was deconvoluted into three peaks with the pristine HESOx at 529, 529.5, and 531.2 eV, which are associated with the surface lattice oxygen (O^{2-}) bound to metals (i.e., metal−oxygen bonds) (O_{lat}), defect sites/surface oxygen species (O_2^{2-}/O^{-}) from low coordinated oxygen atoms or vacancies (O_{vac}), and surface-adsorbed oxygen species such as water molecules (O_{ads}), respectively.[14,15] For both HESOx/OLC and HESOx/OLC$_{AT}$, the peaks of O_{lat}, O_{vac}, and O_{ads} appear at the same peaks of 529.8, 531.7, and 533.2 eV, respectively. The ratio of O_{vac}/O_{lat} (peak area) increases as HESOx/OLC (3.67) < HESOx (4.54) < HESOx/OLC$_{AT}$ (16.07), indicating a higher concentration of surface oxygen vacancies (defects) on the HESOx/OLC$_{AT}$. It has been well established that oxygen vacancies play vital roles in promoting electrocatalytic oxygen reactions (ORR and OER). In the presence of vacant oxygen sites, oxygen species

https://doi.org/10.1021/acs.energyfuels.5c02012
Energy Fuels 2025, 39, 13105−13119

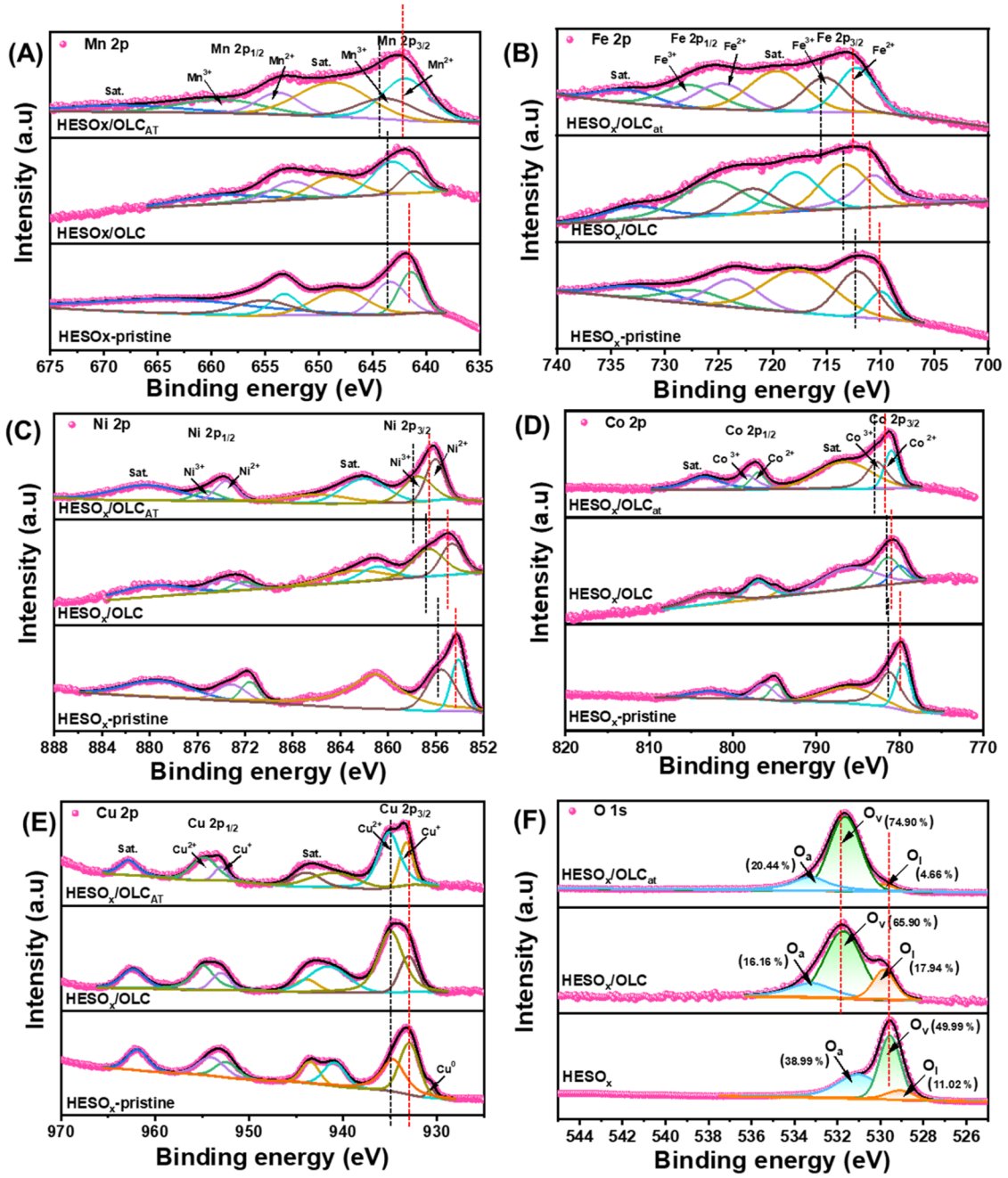

Figure 4. XPS spectra of (A) Mn 2p, (B) Fe 2p, (C) Ni 2p, (D) Co 2p, (E) Cu 2p, and (F) O 1s of the pristine HESOx, HESOx/OLC, and HESOx/OLC$_{AT}$.

can be easily adsorbed and desorbed, thus permitting more efficient mass transport processes to be realized. The deconvoluted C 1s spectra of the three materials (Figure S7) show that the HESOx/OLC$_{AT}$ carbon becomes less graphitic (42.46% sp^2) than the HESOx/OLC (52.60% sp^2). The XPS finding on the existence of oxygen vacancies strongly corroborates the results of both the EPR and Raman experiments.

The nitrogen adsorption−desorption curves of the HESOx samples (Figure S8) depict a characteristic type IV isotherm. From the Brunauer−Emmett−Teller (BET) data (Table S1), HESOx/OLC$_{AT}$ gave the largest BET specific surface area (SBET) of 434.21 m^2 g^{-1}, compared to 387.97 and 14.83 m^2 g^{-1} for HESOx/OLC and pristine HESOx, respectively. From the BET data, HESOx/OLC$_{AT}$, with its high SBET and large pore volume, will have more exposed catalytically active sites for enhanced OER, ORR, and RZAB activities.

Half-Cell Electrochemical Evaluation. The 3-electrode electrochemical experiments were carried out in 1 M KOH, but only for HESOx/OLC and HESOx/OLC$_{AT}$, as the pristine HESOx was insoluble in the ink solvents used for electrode modification. As shown in Figure 5A, the CVs of the HESOx/OLC and HESOx/OLC$_{AT}$ obtained in nitrogen-saturated 1 M KOH solution gave broad redox peaks of similar half-wave potential ($E_{1/2}$ ∼ 0.73 V vs RHE) due to the M(II)/M(III) redox process (where M is most likely due to Mn, Co, and Fe, as Cu is redox-inactive, while Ni redox usually appears at the higher-potential region). The broadness of the redox peak is

https://doi.org/10.1021/acs.energyfuels.5c02012
Energy Fuels 2025, 39, 13105−13119

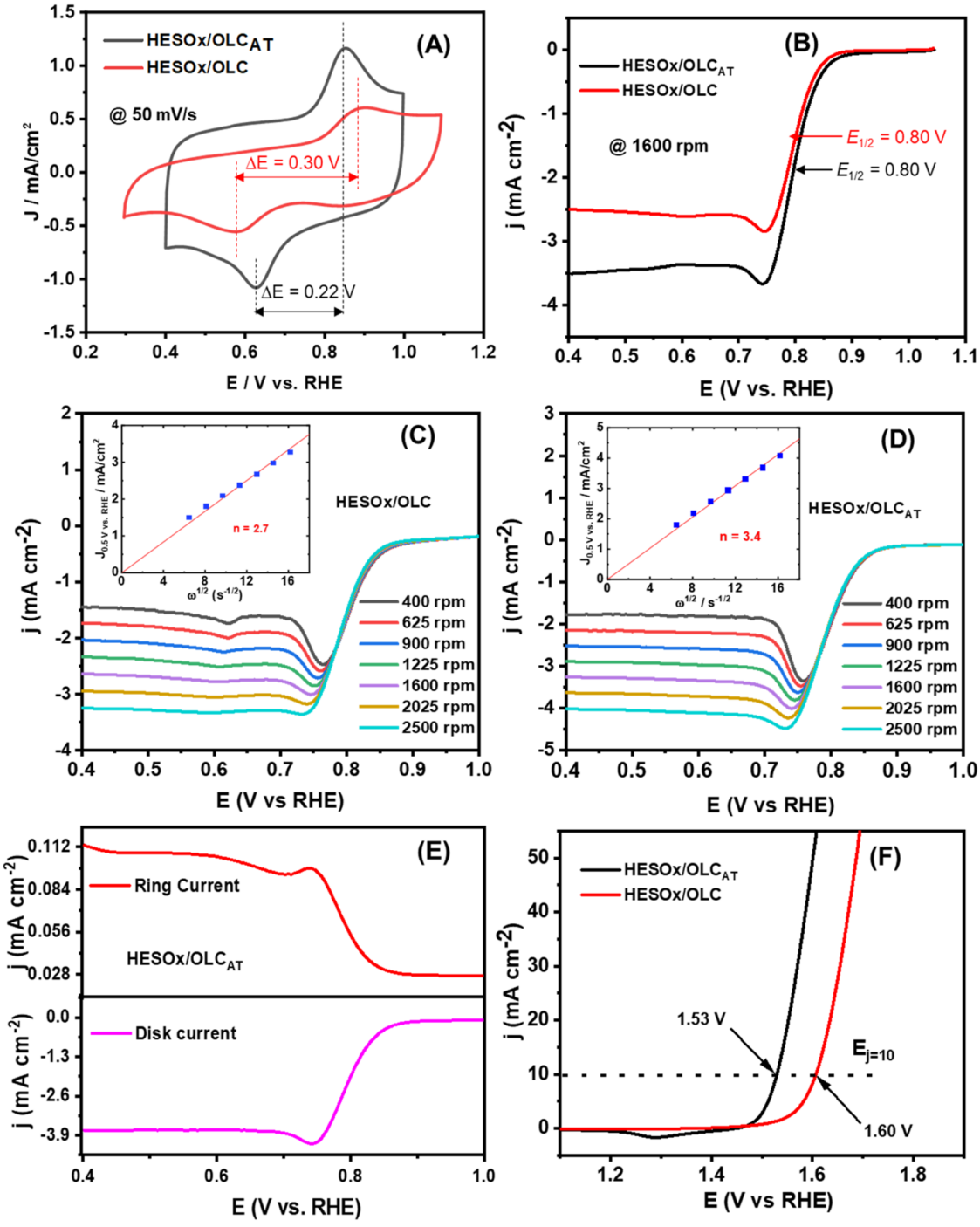

Figure 5. (A) Comparison of the redox processes of HESOx/OLC and HESOx/OLCAT at 50 mV/s in nitrogen-saturated 1 M KOH solution. (B) ORR polarization curves at 1600 rpm in oxygen-saturated 1 M KOH solution. Comparison of the ORR polarization curves for (C) HESOx/OLC and (D) HESOx/OLCAT at different rotation speeds (400−2500 rpm). The insets in (C, D) represent the Koutecky−Levich plots of HESOx/OLC and HESOx/OLCAT, respectively. (E) RRDE voltammograms of HESOx/OLC$_{AT}$ catalysts for the ORR in O_2-saturated 1 M KOH. Ring electrode currents and disk electrode currents are normalized to the geometric surface area of the disk electrode. (F) OER polarization curves at 1600 rpm in O_2-saturated 1 M KOH. Scan rate: 5 mV s^{-1}; rotation rate: 1600 rpm. The catalyst loading was 24 μg_{metal} cm^{-2}, and the ring potential was 1.2 V.

indicative of 2 or more metals involved in the process. The peak-to-peak separation potential (ΔE_p/V) of HESOx/OLC (0.33 V) is larger than that of HESOx/OLC$_{AT}$ (0.22 V), meaning that HESOx/OLC$_{AT}$ exhibits faster electron transfer kinetics than HESOx/OLC. The electrochemical active surface area (ECSA) was determined from the capacitive region of the CV evolutions (Figure S9), calculated as ca. 331 and 405 cm^2 for HESOx/OLC and HESOx/OLCAT, respectively. This trend is consistent with the BET data, corroborating the higher surface area of HESOx/OLC$_{AT}$ over that of its HESOx/OLC counterpart.

In oxygen-saturated KOH electrolyte solution, both catalysts showed well-defined diffusion-limited current densities (j_{lim}) of ca. 0.25 and 3.5 mA cm^{-2} at 1600 r.p.m for HESOx/OLC and

https://doi.org/10.1021/acs.energyfuels.5c02012
Energy Fuels 2025, 39, 13105−13119

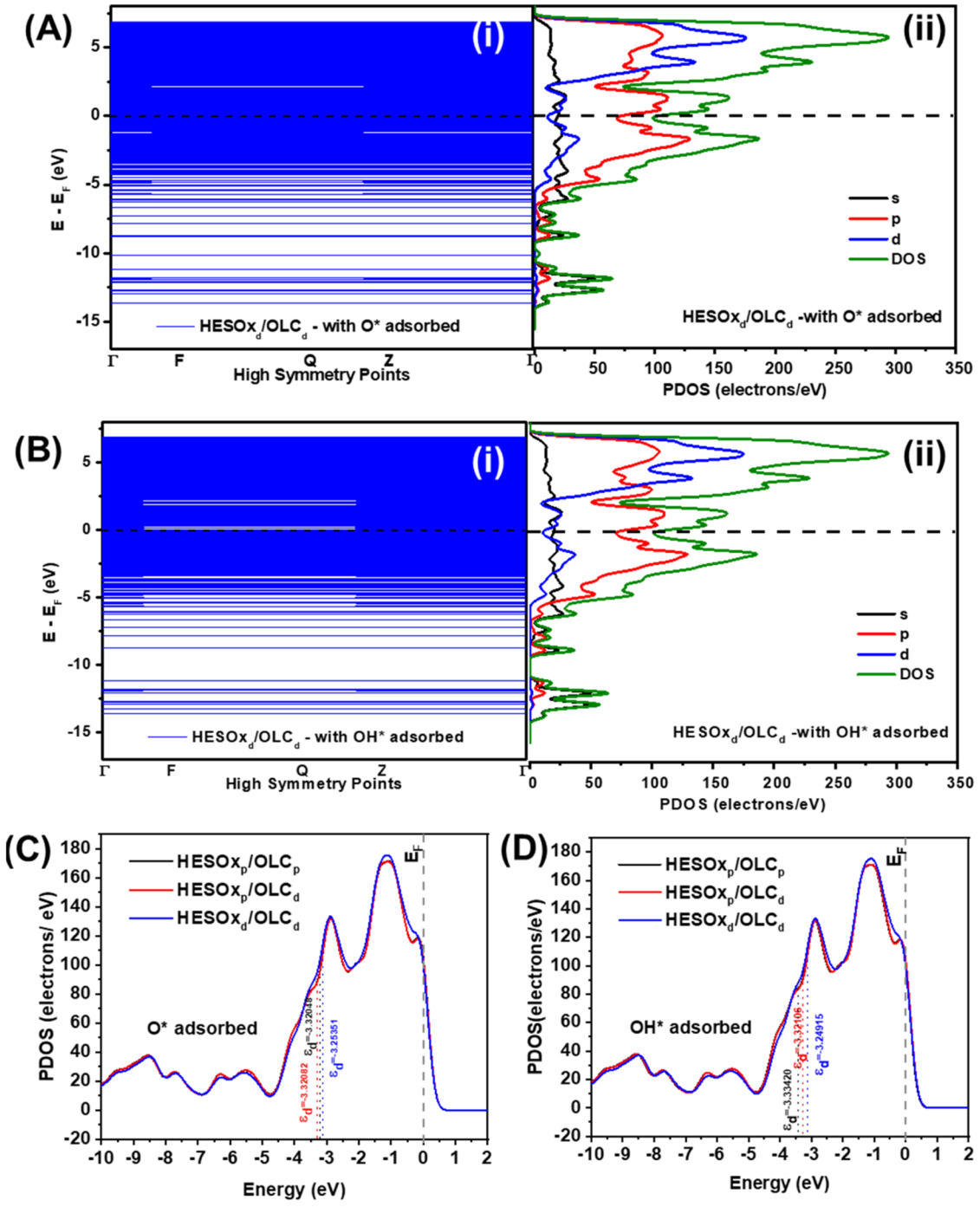

Figure 6. Typical electronic spectroscopic data of the defective $HESOx_d/OLC_d$ (i.e., equivalent of $HESOx/OLC_{AT}$) for the ORR/OER intermediates: (A) O* and (B) OH*. Note that (i) and (ii) represent the band structure and PDOS, respectively. The d-band centers calculated for (C) O* and (D) OH* calculated for the $HESOx_p/OLC_p$, $HESOx_p/OLC_d$, and $HESOx_d/OLC_d$.

$HESOx/OLC_{AT}$, respectively, and similar $E_{1/2}$ values of 0.80 V (Figure 5B). The corresponding Koutecky–Levich (K–L) plots (j^{-1} vs $\omega^{-1/2}$, insets of Figure 5C,D) obtained from the RDE voltammograms at 0.75 V are characterized by excellent linearity ($R^2 \approx 0.99$), meaning first-order reaction kinetics for the ORR as a function of the concentration of dissolved oxygen. The number of transferred electrons at +0.75 V was calculated to be ~2.7 for HESOx/OLC and 3.4 for $HESOx/OLC_{AT}$, confirming the higher ORR activity of $HESOx/OLC_{AT}$ than that of HESOx/OLC. The $HESOx/OLC_{AT}$ catalysts gave better ORR kinetics (Tafel slope of ca. 51 mV dec^{-1}) than HESOx/OLC (Tafel slope of ca. 70 mV dec^{-1}) (Figure S10B). However, both electrocatalysts displayed lower than the 4-electron transport for complete conversion of oxygen to water due to the possibility of H_2O_2 generation. Evaluation of H_2O_2 generation is critical, as H_2O_2 has the potential to deteriorate the performance of fuel cells or metal-air battery membranes. Figure 5E exemplifies typical RRDE voltammograms of the HESOx/OLCAT catalyst in an O_2-saturated 1 M KOH solution. Both ring and disk currents are normalized to the geometric surface area of the disk electrode. The ring current is much smaller (0.10 mA cm^{-2}) than the disk

https://doi.org/10.1021/acs.energyfuels.5c02012
Energy Fuels 2025, 39, 13105−13119

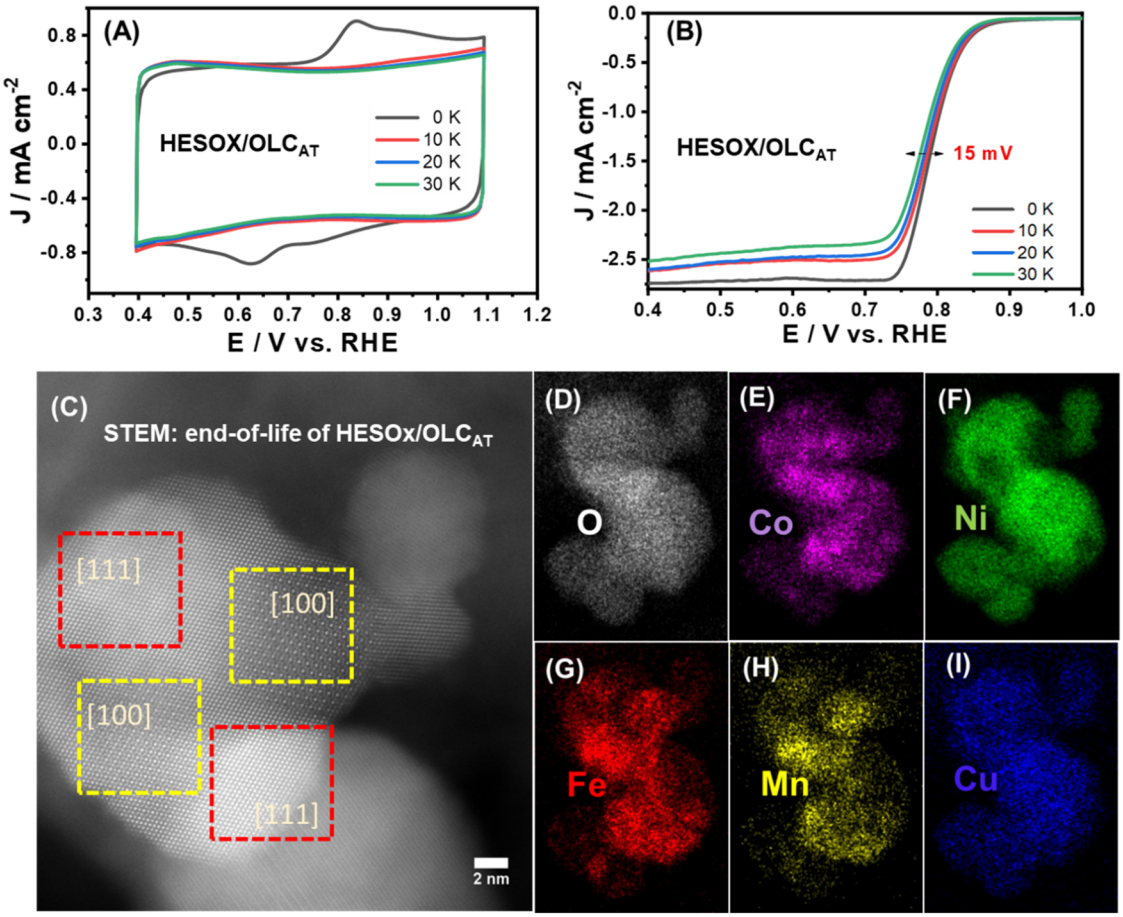

Figure 7. (A) CV and (B) RDE evolutions (1600 rpm) of the HESOx/OLC$_{AT}$ catalyst before and after ADTs (10−30,000 cycles) in oxygen-saturated 1 M KOH at 0.85 V vs RHE. (C) Postmortem analysis: HAADF image at the end-of-life HESOx/OLC$_{AT}$ after ADTs (30,000 cycles) showing no noticeable structural change from its original inverse spinel structure, and (D-I) individual STEM-EDX map of the various elemental composition of the HESOx/OLC$_{AT}$.

current (~3.9 mA cm^{-2}) at ca. 0.75 V and reached a maximum at 0.4 V. The plots of the calculated electron transfer number and the H_2O_2 yield vs potential are shown in Figure S11. The calculated electron transfer number is ~3.0 at 0.75 V, and the H_2O_2 yield was about 50%. Figure 5F compares the OER polarization curves of HESOx/OLC and HESOx/OLC$_{AT}$, with overpotentials of about 370 and 300 mV at 10 mA cm^{-2}, respectively. The HESOx/OLC$_{AT}$ catalysts gave better OER kinetics (Tafel slope of ca. 48 mV dec^{-1}) than HESOx/OLC (Tafel slope of ca. 83 mV dec^{-1}) (Figure S10C).

For application in metal-air batteries such as ReZAB, it is important to determine the "bifunctionality indices (BI)" of these catalysts. Bifunctionality index is a measure of a catalyst's ability to allow both the forward (OER) and reverse (ORR) reactions of the air cathode to occur. The smaller the BI value, the faster the kinetics of the reaction and vice versa. From the results (Figure S10A), it was found that the change in potential (ΔE/V) between ORR and OER follows this sequence: HESOx/OLC$_{AT}$ (ΔE = 0.70 V) < Pt/C-IrO$_2$ (ΔE = 0.75 V) < HESOx/OLC (ΔE = 0.78 V), meaning that the HESOx/OLC$_{AT}$ gave the best electrocatalytic kinetics for application in ReZAB. Indeed, the low-voltage hysteresis of the HESOx/OLC$_{AT}$ is noteworthy[22] and even much lower than generally seen in the current literature that shows >1.0 V.[23]

Theoretical (DFT) Calculations. Although DFT calculation was not the main focus of this work, it was deployed to simply provide some insights into three expected phenomena, i.e., energy band structure, d-band centers, and the d-π hybridization. DFT calculations were carried out using O_2, *O, *OH, and *OOH as adsorbates for ORR and OER. Figure 6 exemplifies the electronic spectroscopic data of the adsorbates on defective HESOx/OLC (i.e., HESOx$_d$/OLC$_d$, representing the HESOx/OLC$_{AT}$) showing the adsorption of O* (Figure 6A) and formation of *OH (Figure 6B) which are generally associated with the intermediates for the rate-determining step for ORR[24,25] and OER,[26,27] respectively. The two prominent bands observed are the d- and p-bands, with the latter dominating due to the high concentration of OLC. The same trend was observed for the other intermediates O2 and *OOH (not shown). The energy band structure of the HESOx/OLC$_{AT}$ is wide, dense, and uniform, which means uniform and well-distributed electronic states.[28] Such a uniform density of states provides reactive sites in catalytic reactions. The wide distribution of electrons means that the electronic interactions between the surface of the HESOx/OLC$_{AT}$ and the reacting intermediates will be diverse, which will bode well for enhanced reactivity of the ORR/OER and catalyst's stability. Such a dense energy band structure indicates the high tunability and responsiveness of the electrons in HESOx/OLC$_{AT}$, which is critical for enhanced electrocatalysis, including fast electron transfer kinetics.

https://doi.org/10.1021/acs.energyfuels.5c02012
Energy Fuels 2025, 39, 13105−13119

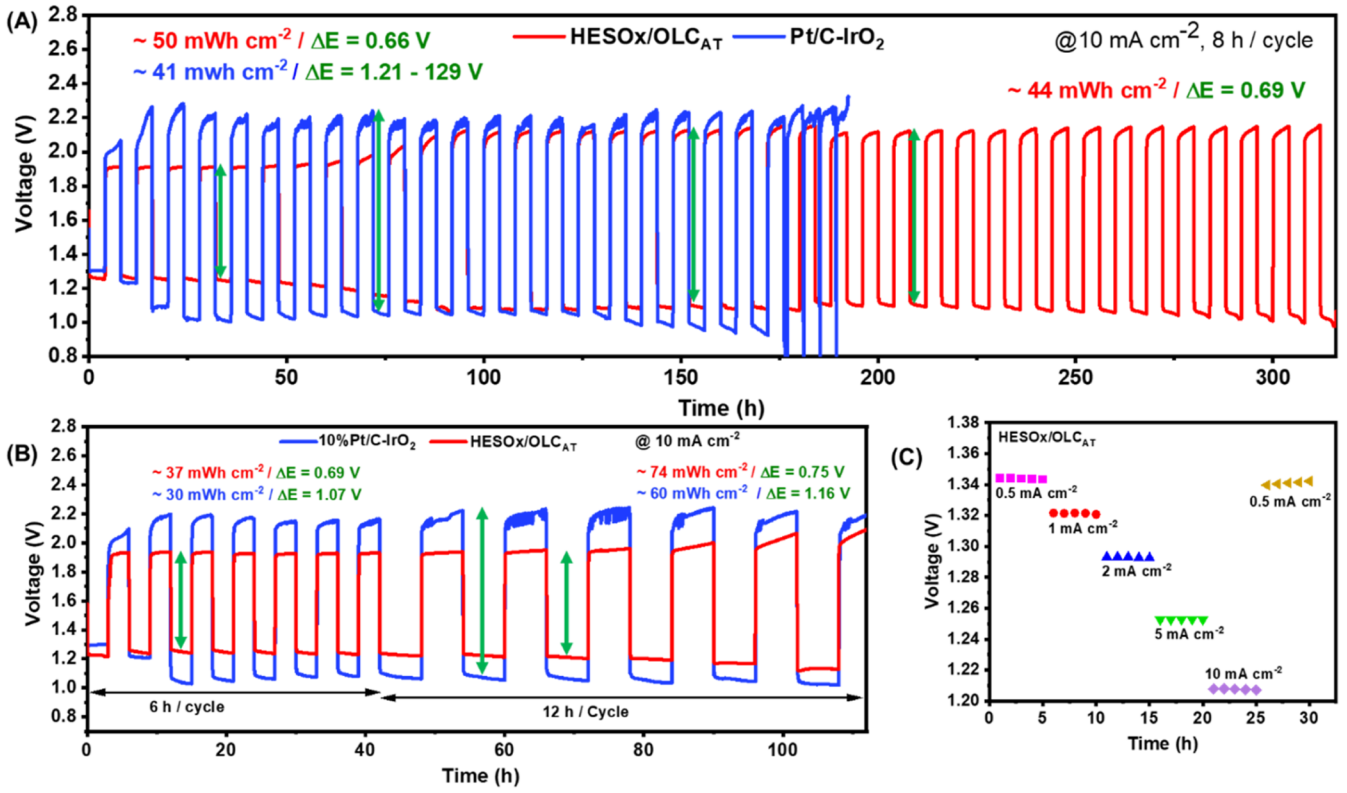

Figure 8. Electrochemical characterizations of HESOx/OLC_{AT} and commercial 10% Pt/C-IrO_2 as air cathodes for aqueous rechargeable zinc−air batteries at 10 mA cm^{-2} current loadings and different discharge areal energy densities: (A) 8 h per cycle, (B) 6 and 12 h per cycles. (C) Rate capability of the ReZAB cell. The double green arrows in (A, B) depict the size of the voltage difference between the charge and discharge cycles (ΔE/V).

The location of the d-band center is the result of the d-π atomic orbital hybridization. The d-band center (ε_d/eV) is one possible determinant of the electrocatalytic activity of transition metal catalysts. The d-band center (ε_d) was calculated according to eq 7[29,30]

$$\varepsilon_d = \frac{\int \rho E dE}{\int \rho dE} \tag{7}$$

where ε_d is the d-band center, ρ is the density of the d-band, E is the energy of the d-band, and ρdE represents the number of states.

Figure 6C,D compares the respective d-band centers of the *O and *OH calculated for the $HESOx_p/OLC_p$, $HESOx_p/OLC_d$, and $HESOx_d/OLC_d$. To improve the ORR and OER activities, the d-band center of surface HESOx must be downshifted, which, in principle, can be realized if the transition metals in HESOx are further oxidized as already shown via the XPS data. As shown in the Supporting Information (Table S2), the d-band centers for HESOx are much stronger (around −1.9 eV) than the OLC-based HESOx (around −3.3 eV) for each of the intermediates. Interestingly, however, the d-band centers recorded at the $HESOx_d/OLC_d$ surface for *O (−3.25351 eV) and *OH (−3.24195 eV) are slightly more positive (i.e., slightly stronger adsorption, being closer to the Fermi level) than the other electrocatalysts studied in this work. The reason for this slight deviation from the d-band theory has been observed by other workers and was attributed to the ability of the adsorbate to adsorb at different sites on the catalyst.[29,31,32] Thus, it is highly probable that this could be happening in our case, too, especially considering the inherent ability of high-entropy electrocatalysts to provide multiple catalytic sites for intermediates coupled with the highly defective nature of the HESOx/OLC_{AT} catalyst studied in this work.

Accelerated Degradation Test (ADT). Based on the high electrocatalytic performance of HESOx/OLC_{AT} toward the ORR and the OER processes, all further studies were focused on the HESOx/OLC_{AT} catalyst. First, we investigated its ORR electrochemical durability via an accelerated degradation test (ADT). As shown in Figure 7A, the initial CV showed two broad redox peaks that disappeared after 10,000 cycles. From the 10,000th cycle, a rectangular CV shape, characteristic of capacitive behavior, was observed until the 30,000th cycle, demonstrating a remarkable enhancement in stability.

As exhibited in Figure 7B, the HESOx/OLC_{AT} catalyst showed an activity decay with a $\Delta E_{1/2}$ value of 15 mV after 30,000 cycles. To interrogate the reason for the enhanced electrocatalytic activity, HAADF-STEM characterization (Figures 7C and S12) was further carried out to examine the size, morphology, and crystal phase changes. Impressively, after the ADT of 30,000 cycles, the HESOx/OLC_{AT} catalyst retained its pristine inverse spinel structural properties, with EDX mappings (Figure 7D−I) showing uniform elemental distribution. Furthermore, using chronoamperometry to test the OER stability (Figure S13), it was shown that the HESOx/OLC_{AT} maintained a constant voltage of 1.53 V for the 10 h duration, while the $HESO_x$/OLC showed a higher voltage (1.66 V) and quickly degraded after 6 h. This result proves that the $HESO_x$/

https://doi.org/10.1021/acs.energyfuels.5c02012
Energy Fuels 2025, 39, 13105−13119

OLC_{AT} catalyst is more electrochemically robust than the $HESO_x$/OLC.

Evaluation of Rechargeable Zinc−Air Battery for Technological Application. Figure S14 exemplifies typical discharge polarization curves of HESOx/OLC and HESOx/OLC_{AT} with satisfactory power densities of 139 and 152 mW cm^{-2}, respectively (Figure S14A). Figure S14B shows typical discharge−charge polarization curves of the HESOx/OLC_{AT} for the RZAB at a constant current density of 2 mA cm^{-2} carried out for up to 300 cycles. Also, discharge−charge experiments were conducted for the ReZAB cell at 2 mA cm^{-2} and low cycling time of 1 h per cycle (i.e., shallow cycling), which exhibited long-hour cycling (>300 h) and good kinetics (ΔE = 58−74 mV) (Figure S15). Shallow cycling for ReZAB cells, as shown in Figure S15, provides no useful data for real application. Disappointingly, however, shallow cycling (as low as 10 min per cycle) is what is mostly reported in the literature to prove "high-performance" for both conventional electrocatalysts[33−36] and high-entropy electrocatalysts[28,32,37−40] (also see Table S3 and references therein). It cannot be overemphasized that shallow cycling alone should not be used to prove excellence in performance. This is why, for technological relevance, Rolison and co-workers[2] recommended the need for ReZAB to be subjected to deep cycling at a current loading of 10 mA cm^{-2} and at 35 mWh cm^{-2} to be able to compete with Li-ion battery pack.[2]

In this work, the HESOx-based ReZAB was fabricated with a polished zinc plate as the anode, HESOx material as the cathode, and an alkaline aqueous electrolyte (6 M KOH + 0.2 M zinc acetate). For comparison, a ReZAB with commercial Pt−C/IrO_2 as the air cathode catalyst was also assembled. Figure 8 compares the electrochemical properties of the ReZAB studied in this work using HESOx/OLC_{AT} and commercial 10% Pt/C-IrO_2 as air cathode electrocatalysts at 10 mA cm^{-2} current loading and different discharge areal energy densities of (A) 8 h per cycle and (B) 6 and 12 h per cycles. The double green arrow indicates the voltage difference between the charge and discharge cycles (ΔE/V).

As seen from Figure 8A,B, the ReZAB can be discharged at higher areal energy density (37−74 mWh cm^{-2}) than the recommended threshold of discharge areal energy density (35 mWh cm^{-2}) and at excellent kinetics (ΔE = 0.66−75 V). In contrast, the highly expensive commercial dual-catalyst (Pt/C-IrO_2) is unstable (crashes very easily) with poor kinetics (ΔE = 1.07−1.29 V). Figure 8C is the rate capability plot of the ReZAB cell, which reveals that the battery cell can be charged and discharged at different current densities. The results reported here for ReZAB compare with, and are even better, than the best 8% articles that were reported to have met the minimum threshold for real technological applications (please see Hopkins et al.[2] for details). In addition, Table S3 compares the performance of HESOx/OLC_{AT} with some of the medium- to high-entropy material-based air-breathing catalysts used for ReZABs.[38,39,41−72] It is clearly seen in Table S3 that most electrocatalysts use shallow discharge cycling (5−30 min) for ReZAB and expectedly achieved high number of cycles (as we also show in this work, see Figure S15), HESOx/OLC_{AT} achieved the rarely reported deep cycling (3−6 h) that would potentially allow for device applications. Indeed, the HESOx/OLCAT exhibits the most significant enhancement of a ReZAB yet reported.

CONCLUSIONS

Single nanocrystals of inverse-type high-entropy spinel oxides confined in highly curved defective onion-like carbons (HESOx/OLC_{AT}) have been successfully synthesized and characterized. The synthesis method adopted here results in controlled defective engineering (oxygen vacancies), strong electronic interaction between the OLC and HESOx, characterized by unique surface "tip" exposure of the metallic elements that allows for efficient electron transport from the metallic elements to the OLC species, and weak d-band centers of the component transition metals. The excellent electrocatalytic properties of defect-rich HESOx/OLC_{AT} toward ORR/OER and ReZAB are related to the strong electronic modulation arising from d-π hybridization and weakened d-band centers in the HESOx/OLC_{AT} complex. The level of electron transfer is more pronounced with Fe and less significant with Cu. It is shown that the ORR/OER activities in alkaline electrolyte are governed by the excellent electronic modulation of the defect-rich HESOx/OLC_{AT} catalyst with multiple catalytic sites for intermediates and weakened d-band centers of the rate-determining intermediates (i.e., *O adsorption for ORR and *OOH formation for the OER) compared to the pristine HESOx. The HESOx/OLC_{AT} showed excellent electrochemical cycling stability, proven by stable structural properties before and at end-of-life. The HESOx/OLC_{AT} catalyst was used to fabricate and test for application in ReZAB, and the battery was able to be continuously charged and discharged at a 10 mA cm^{-2} current load, yielding high areal energy densities between 37 and 74 mWh $cm_{geometric}^{-2}$. This result outperforms the literature-recommended threshold of 35 mWh $cm_{geometric}^{-2}$ for technological applications and represents one of the top performers for ReZAB reported. In the future, there will be a need to demonstrate this work using commercial-sized ReZAB cells.

ASSOCIATED CONTENT

Supporting Information

The Supporting Information is available free of charge at https://pubs.acs.org/doi/10.1021/acs.energyfuels.5c02012.

Synthesis scheme for HESOx, HESOx/OLC, and HESOx/OLCAT; fabrication of the ReZAB cells; description of the computational studies; associated images and data for TGA, HRTEM, HRSEM, BET/Nitrogen adsorption/desorption curves; measurements of double-layer capacitance to determine the ECSA, ORR/OER bifunctional curves, and Tafel slopes for the catalysts; electron transfer number and amount of hydrogen peroxide (H_2O_2) produced in an alkaline medium for HESOx/OLCAT; STEM of the HESOx/OLCAT at the end-of-life HESOx/OLCAT after ADTs (30k cycles) showing no noticeable structural change from its original inverse spinel structure; long-term cycling tests, including chronoamperograms at 10 mA cm^{-2} for 10 h; discharge polarization curves and corresponding power density curves of the ReZAB based on the HESOx/OLC and HESOx/OLC_{AT} from LSV, typical discharge−charge polarization curves of the HESOx/OLC_{AT} based RZAB at a current density of 2 mA cm^{-2} between 5 and 300 cycles; discharge−charge curves of HESOx/OLC_{AT} and 10% Pt/C-IrO_2 at a current density of 2 mA cm^{-2} for 1 h per cycle; tables

https://doi.org/10.1021/acs.energyfuels.5c02012
Energy Fuels 2025, 39, 13105−13119

showing Brunauer−Emmett−Teller (BET) data for the HESOx materials; summary of the d-band centers for ORR/OER intermediates; and survey of several recent literature (including this work) on rechargeable zinc−air batteries showing how this work outperforms most literature, especially in terms of areal-discharge energy density (PDF)

AUTHOR INFORMATION

Corresponding Authors

Héctor D. Abruña − *Department of Chemistry and Chemical Biology, Cornell University, Ithaca, New York 14850, United States;* orcid.org/0000-0002-3948-356X; Email: hda1@cornell.edu

Kenneth I. Ozoemena − *School of Chemistry, Molecular Sciences Institute, University of the Witwatersrand, Johannesburg 2050, South Africa;* orcid.org/0000-0001-7107-7003; Email: Kenneth.ozoemena@wits.ac.za

Authors

Agnes Mongwe − *School of Chemistry, Molecular Sciences Institute, University of the Witwatersrand, Johannesburg 2050, South Africa*

Aderemi B. Haruna − *School of Chemistry, Molecular Sciences Institute, University of the Witwatersrand, Johannesburg 2050, South Africa*

Lesego Gaolatlhe − *School of Chemistry, Molecular Sciences Institute, University of the Witwatersrand, Johannesburg 2050, South Africa*

Joesene Soto − *Department of Chemistry and Chemical Biology, Cornell University, Ithaca, New York 14850, United States; Kavli Institute at Cornell for Nanoscale Science, Cornell University, Ithaca, New York 14850, United States*

Zixiao Shi − *Kavli Institute at Cornell for Nanoscale Science and School of Applied and Engineering Physics, Cornell University, Ithaca, New York 14850, United States*

Patrick V. Mwonga − *School of Chemistry, Molecular Sciences Institute, University of the Witwatersrand, Johannesburg 2050, South Africa*

Xiao-Yu Yang − *School of Chemistry, Molecular Sciences Institute, University of the Witwatersrand, Johannesburg 2050, South Africa; State Key Laboratory of Advanced Technology for Materials Synthesis and Processing, School of Materials Science and Engineering, Wuhan University of Technology, Wuhan 430070, China;* orcid.org/0000-0002-0880-9790

David A. Muller − *Kavli Institute at Cornell for Nanoscale Science and School of Applied and Engineering Physics, Cornell University, Ithaca, New York 14850, United States*

Complete contact information is available at: https://pubs.acs.org/10.1021/acs.energyfuels.5c02012

Notes

The authors declare no competing financial interest.

ACKNOWLEDGMENTS

This work was supported by the SASOL-NRF University Collaborative Research Grant for the project on the *"Development of Robust and Low-Cost High Energy Rechargeable Zinc-Air Batteries"* (UID:138628), the DSTI/NRF/Wits SARChI Chair on *Materials Electrochemistry and Energy Technologies* (MEET) (UID #132739), and the DSTI Energy Storage Consortium grant. AM thanks SASOL-NRF for the MSc scholarship. K.I.O. is grateful to HDA and Cornell University's *Centre for Alkaline-Based Energy Solutions* (CABES), part of the Energy Frontier Research Center (EFRC) program supported by the U.S. Department of Energy, under grant DE-SC-0019445, for hosting and supporting his 1-year sabbatical leave. J.S. acknowledges support by the Cornell Energy Systems Institute (CESI) and the Kavli Institute at Cornell (KIC).

REFERENCES

(1) Chervin, C.; Long, J.; Parker, J.; Rolison, D. *Rechargeable Zn-Air Batteries with Pulse-Power Capability*; Naval Research Laboratory: Washington DC, USA, 2020.

(2) Hopkins, B. J.; Chervin, C. N.; Parker, J. F.; Long, J. W.; Rolison, D. R. An areal-energy standard to validate air-breathing electrodes for rechargeable zinc−air batteries. *Adv. Energy Mater.* **2020**, *10* (30), No. 2001287.

(3) Hopkins, B. J.; Chervin, C. N.; Parker, J. F.; Long, J. W.; Rolison, D. R. Electrocatalyst or support? Circumventing corrosion for long-lived zinc−air batteries. *Next Energy* **2023**, *1* (4), No. 100054.

(4) Bao, K.-L.; Xu, J.-Y.; Yu, N.-F.; Kuang, J.-B.; Yang, Z.-T.; Chen, H.; Ye, J.-L.; Wu, Y.-P. Oxygen Defect-Enriched Hierarchical NiCo2O4 Hollow Rectangular Nanobars with Enhanced Bifunctional Oxygen Electrocatalysis for Efficient Rechargeable Zinc−Air Batteries. *Energy Fuels* **2022**, *36* (12), 6542−6551.

(5) Fu, D.; Zhu, Z.; Gao, S.; Qi, H.; Liu, X.; Liu, W.; Zeng, S. Hollow Co/N-C@NiCo2O4 Spheres as Highly Efficient Bifunctional Oxygen Electrocatalysts for Rechargeable Zinc−Air Batteries. *Energy Fuels* **2023**, *37* (15), 11319−11331.

(6) Bao, L.; Bao, C.; Sun, Q.; Zou, J.; Liu, H.; HuiChen. Hierarchical Porous Carbon with N/S Codoped Bimetal as a High-Efficiency Oxygen Reduction Catalyst for Rechargeable Zinc−Air Batteries. *Energy Fuels* **2023**, *37* (23), 19137−19146.

(7) Zhang, X.; Liu, Y.; Zhao, X.; Cheng, Z.; Mu, X. Recent Advances and Perspectives of High-Entropy Alloys as Electrocatalysts for Metal-Air Batteries. *Energy Fuels* **2024**, *38* (20), 19236−19252.

(8) Ipadeola, A. K.; Haruna, A. B.; Gaolatlhe, L.; Lebechi, A. K.; Meng, J.; Pang, Q.; Eid, K.; Abdullah, A. M.; Ozoemena, K. I. Efforts at Enhancing Bifunctional Electrocatalysis and Related Events for Rechargeable Zinc-Air Batteries. *ChemElectroChem* **2021**, *8* (21), 3998−4018.

(9) Haruna, A. B.; Ozoemena, K. I. Manganese-based bifunctional electrocatalysts for zinc-air batteries. *Curr. Opin. Electrochem.* **2020**, *21*, 219−224.

(10) Jafta, C. J.; Mathe, M. K.; Manyala, N.; Roos, W. D.; Ozoemena, K. I. Microwave-assisted synthesis of high-voltage nanostructured LiMn1. 5Ni0. 5O4 spinel: tuning the Mn3+ content and electrochemical performance. *ACS Appl. Mater. Interfaces* **2013**, *5* (15), 7592−7598.

(11) Wang, Y.; Li, H.; Liu, H.; Yang, L.; Zeng, C. Preparation and formation mechanism of Cr-free spinel-structured high entropy oxide (MnFeCoNiCu) 3O4. *Ceram. Int.* **2023**, *49* (2), 1940−1946.

(12) Liu, D.; Li, X.; Chen, S.; Yan, H.; Wang, C.; Wu, C.; Haleem, Y. A.; Duan, S.; Lu, J.; Ge, B.; et al. Atomically dispersed platinum supported on curved carbon supports for efficient electrocatalytic hydrogen evolution. *Nat. Energy* **2019**, *4* (6), 512−518.

(13) Wen, H.; Zhao, Z.; Luo, Z.; Wang, C. Unraveling the impact of curvature on electrocatalytic performance of carbon materials: a state-of-the-art review. *ChemSusChem* **2024**, *17* (10), No. e202301859.

(14) Gioria, E.; Li, S.; Mazheika, A.; Naumann d'Alnoncourt, R.; Thomas, A.; Rosowski, F. CuNi nanoalloys with tunable composition and oxygen defects for the enhancement of the oxygen evolution reaction. *Angew. Chem.* **2023**, *135* (26), No. e202217888.

(15) Liu, L.; Ji, Y.; You, W.; Liu, S.; Shao, Q.; Kong, Q.; Hu, Z.; Tao, H.; Bu, L.; Huang, X. Trace Lattice S Inserted RuO2 Flexible Nanosheets for Efficient and Long-Term Acidic Oxygen Evolution Catalysis. *Small* **2023**, *19* (38), No. 2208202.

(16) Zhang, M.; Duan, X.; Gao, Y.; Zhang, S.; Lu, X.; Luo, K.; Ye, J.; Wang, X.; Niu, Q.; Zhang, P.; Dai, S. Tuning oxygen vacancies in oxides by configurational entropy. *ACS Appl. Mater. Interfaces* **2023**, *15* (39), 45774−45789.
(17) Schmitt, R.; Kubicek, M.; Sediva, E.; Trassin, M.; Weber, M. C.; Rossi, A.; Hutter, H.; Kreisel, J.; Fiebig, M.; Rupp, J. L. Accelerated ionic motion in amorphous memristor oxides for nonvolatile memories and neuromorphic computing. *Adv. Funct. Mater.* **2019**, *29* (5), No. 1804782.
(18) Zhang, J.; Liu, H.; Gu, Y.; Zhang, J.; Zhang, X.; Qi, X. Oxygen-vacancy-related dielectric relaxations and electrical properties in [Li x (BaSrCaMg)(1− x)/4] TiO3 high-entropy perovskite ceramics. *J. Mater. Sci.: Mater. Electron.* **2022**, *33* (13), 9918−9929.
(19) Ozgur, C.; Erdil, T.; Geyikci, U.; Okuyucu, C.; Lokcu, E.; Kalay, Y. E.; Toparli, C. Engineering Oxygen Vacancies in (FeCrCoMnZn) 3O4-δ High Entropy Spinel Oxides Through Altering Fabrication Atmosphere for High-Performance Rechargeable Zinc-Air Batteries. *Global Challenges* **2024**, *8* (1), No. 2300199.
(20) Ogada, J. J.; Ipadeola, A. K.; Mwonga, P. V.; Haruna, A. B.; Nichols, F.; Chen, S.; Miller, H. A.; Pagliaro, M. V.; Vizza, F.; Varcoe, J. R.; et al. CeO2Modulates the Electronic States of a Palladium Onion-Like Carbon Interface into a Highly Active and Durable Electrocatalyst for Hydrogen Oxidation in Anion-Exchange-Membrane Fuel Cells. *ACS Catal.* **2022**, *12*, 7014−7029.
(21) Ogada, J. J.; Ehirim, T. J.; Ipadeola, A. K.; Haruna, A. B.; Mwonga, P. V.; Abdullah, A. M.; Yang, X.-Y.; Eid, K.; Wamwangi, D. M.; Ozoemena, K. I. Interfacial Electronic Interactions within the Pd-CeO2/Carbon Onions Define the Efficient Electrocatalytic Ethanol Oxidation Reaction in Alkaline Electrolytes. *ACS Omega* **2024**, *9* (7), 7439−7451.
(22) Chervin, C. N.; Hopkins, B. J.; Hoffmaster, A. N.; Skeele, N. L.; Ko, J. S.; Parker, J. F.; Hudak, B. M.; Long, J. W.; Rolison, D. R. Sustainable Electrocatalytic Architectures Enable Rechargeable Zinc−Air Batteries with Low Voltage Hysteresis. *ACS Appl. Energy Mater.* **2020**, *3* (11), 10485−10494.
(23) Erdil, T.; Toparli, C. B-site effect on high-entropy perovskite oxide as a bifunctional electrocatalyst for rechargeable zinc−air batteries. *ACS Appl. Energy Mater.* **2023**, *6* (21), 11255−11267.
(24) Yang, Y.; Qi, W.; Niu, J.; Chen, F.; Li, W. Understanding active sites and mechanism of oxygen reduction reaction on FeN4−doped graphene from DFT study. *Int. J. Hydrogen Energy* **2020**, *45* (31), 15465−15475.
(25) Xiao, B. B.; Jiang, X.; Jiang, Q. Density functional theory study of oxygen reduction reaction on Pt/Pd 3 Al (111) alloy electrocatalyst. *Phys. Chem. Chem. Phys.* **2016**, *18* (21), 14234−14243.
(26) Huang, T.; Guo, M.; Li, W.; Bao, Y.; Yu, A.; Li, D.-S.; Tu, J.; Wang, M.; Hao, W.; Sun, C. High-performance oxygen evolution reaction via self-optimizing interface engineering with simultaneous activation of dual-sites of surface oxyhydroxides. *Appl. Surf. Sci.* **2024**, *659*, No. 159936.
(27) Romeo, E.; Illas, F.; Calle-Vallejo, F. A general but still unknown characteristic of active oxygen evolution electrocatalysts. *Chem. Sci.* **2023**, *14* (13), 3622−3629.
(28) Yang, B.; Bao, C.; Zhai, L.; Xiang, Z. High-entropy spinel oxides coupling with covalent organic polymers as bifunctional oxygen electrocatalysts for zinc-air batteries. *Chem. Eng. J.* **2025**, *515*, No. 163757.
(29) Fan, T.-E.; Demiroglu, I.; Hussein, H. A.; Liu, T.-D.; Johnston, R. L. DFT study of the structure, chemical ordering and molecular adsorption of Pd−Ir nanoalloys. *Phys. Chem. Chem. Phys.* **2017**, *19* (39), 27090−27098.
(30) Hammer, B.; Nørskov, J. K. Theoretical Surface Science and Catalysis—Calculations and Concepts. In *Advances in Catalysis*; Elsevier, 2000; Vol. *45*, pp 71−129.
(31) Stamenkovic, V.; Mun, B. S.; Mayrhofer, K. J.; Ross, P. N.; Markovic, N. M.; Rossmeisl, J.; Greeley, J.; Nørskov, J. K. Changing the activity of electrocatalysts for oxygen reduction by tuning the surface electronic structure. *Angew. Chem., Int. Ed.* **2006**, *45* (18), 2897−2901.
(32) Jiang, P.; Xu, Y.; Gong, Z.; Ge, B.; Ding, L.; Huang, C.; Qiu, X.; Pei, Z. Entropy-Driven Competitive Adsorption Sites Tailoring Unlocks Efficient Hybrid Conversion Zn−Air Batteries. *Angew. Chem.* **2025**, *137*, No. e202504188.
(33) Wang, P.; Deng, D.; Wu, S.; Xu, L. Cobalt-based deep eutectic solvent modified nitrogen-doped carbon catalyst for boosting oxygen reduction reaction in zinc-air batteries. *Chin. J. Struct. Chem.* **2024**, *43* (1), No. 100199.
(34) Liu, Y.; Liu, S.; Zhang, P.; Zhou, J.; Liu, H.; Li, S.; Li, X.; Wang, X.; Han, D.; Chen, Y. Electronic Structure Regulation of MnCo2O4 via Surface-Phosphorization Coupling to Monolithic Carbon for Oxygen Electrocatalysis in Zn−Air Batteries. *Adv. Funct. Mater.* **2024**, *34* (41), No. 2400522.
(35) Zhu, J.; Chen, J.; Li, X.; Luo, K.; Xiong, Z.; Zhou, Z.; Zhu, W.; Luo, Z.; Huang, J.; Li, Y. Steering surface reconstruction of hybrid metal oxides for efficient oxygen evolution reaction in water splitting and zinc-air batteries. *J. Energy Chem.* **2024**, *92*, 383−393.
(36) Ye, L.; Chen, W.; Jiang, Z. J.; Jiang, Z. Co/CoO heterojunction rich in oxygen vacancies introduced by O2 plasma embedded in mesoporous walls of carbon nanoboxes covered with carbon nanotubes for rechargeable zinc−air battery. *Carbon Energy* **2024**, *6* (7), No. e457.
(37) Xie, M.; Lu, Y.; Xiao, X.; Wu, D.; Shao, B.; Nian, H.; Wu, C.; Wang, W.; Gu, J.; Han, S.; et al. Spatially immobilized PtPdFeCoNi as an excellent bifunctional oxygen electrocatalyst for zinc−air battery. *Adv. Funct. Mater.* **2025**, *35* (5), No. 2414537.
(38) Li, W.; Wang, Y.; Xu, N.; Li, Y. High-entropy spinel oxides as efficient ORR catalysts towards enhanced kinetics for zinc-air batteries. *J. Energy Storage* **2025**, *123*, No. 116784.
(39) Qiu, Z.; Guo, X.; Cao, S.; Du, M.; Wang, Q.; Pi, Y.; Pang, H. High-Entropy Ag− Ru-Based Electrocatalysts with Dual-Active-Center for Highly Stable Ultra-Low-Temperature Zinc-Air Batteries. *Angew. Chem., Int. Ed.* **2025**, *64* (3), No. e202415216.
(40) Li, J.; Li, B.; Li, P.-T.; Zhang, N.; Shang, H.-S. A ZnFeNiCoCr high-entropy alloy for efficient bifunctional oxygen electrocatalysis. *Rare Met.* **2025**, *44* (3), 1789−1799.
(41) Zhai, W.; He, Y.; Duan, Y.-e.; Guo, S.; Chen, Y.; Dai, Z.; Liu, L.; Tan, Q. Densely populated trimetallic single-atoms for durable low-temperature flexible zinc-air batteries. *Appl. Catal., B* **2024**, *342*, No. 123438.
(42) Chen, S.; Xu, J.; Chen, J.; Yao, Y.; Wang, Z.; Li, P.; Li, Y.; Wang, F. Ru doping induced interface engineering in flower-liked CoMoO4-RuO2 boosts oxygen electrocatalysis for rechargeable Zn-air battery. *J. Colloid Interface Sci.* **2024**, *658*, 230−237.
(43) Niu, Y.; Jiang, G.; Gong, S.; Liu, X.; Shangguan, E.; Li, L.; Chen, Z. Engineering of heterointerface of ultrathin carbon nanosheet-supported CoN/MnO enhances oxygen electrocatalysis for rechargeable Zn−air batteries. *J. Colloid Interface Sci.* **2024**, *656*, 346−357.
(44) Wang, L.; Hu, X.; Li, H.; Huang, Z.; Huang, J.; Isimjan, T. T.; Yang, X. Engineering built-in electric fields in oxygen-deficient MnO-CeO 2@ Cs catalysts: enhanced performance and kinetics for the oxygen reduction reaction in aqueous/flexible zinc−air batteries. *Green Chem.* **2024**, *26* (4), 2011−2020.
(45) Gao, L.; Zhong, X.; Li, Z.; Hu, J.; Cui, S.; Wang, X.; Xu, B. A multi-layer reduced graphene oxide catalyst encapsulating a high-entropy alloy for rechargeable zinc-air batteries. *Chem. Commun.* **2024**, *60* (10), 1269−1272.
(46) He, R.; Yang, L.; Zhang, Y.; Wang, X.; Lee, S.; Zhang, T.; Li, L.; Liang, Z.; Chen, J.; Li, J.; et al. A CrMnFeCoNi high entropy alloy boosting oxygen evolution/reduction reactions and zinc-air battery performance. *Energy Storage Mater.* **2023**, *58*, 287−298.
(47) Cao, X.; Gao, Y.; Wang, Z.; Zeng, H.; Song, Y.; Tang, S.; Luo, L.; Gong, S. FeNiCrCoMn high-entropy alloy nanoparticles loaded on carbon nanotubes as bifunctional oxygen catalysts for rechargeable zinc-air batteries. *ACS Appl. Mater. Interfaces* **2023**, *15* (27), 32365−32375.
(48) Yao, Y.; Li, Z.; Dou, Y.; Jiang, T.; Zou, J.; Lim, S. Y.; Norby, P.; Stamate, E.; Jensen, J. O.; Zhang, W. High entropy alloy nanoparticles

encapsulated in graphitised hollow carbon tubes for oxygen reduction electrocatalysis. *Dalton Trans.* **2023**, *52* (13), 4142−4151.
(49) Zhang, Q.; Lian, K.; Liu, Q.; Qi, G.; Zhang, S.; Luo, J.; Liu, X. High entropy alloy nanoparticles as efficient catalysts for alkaline overall seawater splitting and Zn-air batteries. *J. Colloid Interface Sci.* **2023**, *646*, 844−854.
(50) Arafat, Y.; Zhong, Y.; Azhar, M. R.; Asif, M.; Tadé, M. O.; Shao, Z. CoNiFe-layered double hydroxide decorated Co-N-C network as a robust bi-functional oxygen electrocatalyst for zinc-air batteries. *EcoMat* **2023**, *5* (10), No. e12394.
(51) Dang, L.; Zhang, K.; Wang, Q.; Xu, C.; Wang, S. Fe-Alloyed MoNi Nanohybrids as Oxygen Evolution Reaction/Oxygen Reduction Reaction Bifunctional Electrocatalyst for Rechargeable Zinc−Air Batteries. *Phys. Status Solidi A* **2023**, *220* (2), No. 2200581.
(52) Yu, T.; Xu, H.; Jin, Z.; Zhang, Y.; Qiu, H.-J. Noble metal-free high-entropy oxide/Co-NC bifunctional electrocatalyst enables highly reversible and durable Zn-air batteries. *Appl. Surf. Sci.* **2023**, *610*, No. 155624.
(53) Jin, Z.; Zhou, X.; Hu, Y.; Tang, X.; Hu, K.; Reddy, K. M.; Lin, X.; Qiu, H.-J. A fourteen-component high-entropy alloy@ oxide bifunctional electrocatalyst with a record-low Δ E of 0.61 V for highly reversible Zn−air batteries. *Chem. Sci.* **2022**, *13* (41), 12056−12064.
(54) Lin, X.; Hu, Y.; Hu, K.; Lin, X.; Xie, G.; Liu, X.; Reddy, K. M.; Qiu, H.-J. Inhibited surface diffusion of high-entropy nano-alloys for the preparation of 3D nanoporous graphene with high amounts of single atom dopants. *ACS Mater. Lett.* **2022**, *4* (5), 978−986.
(55) Jin, Z.; Lyu, J.; Hu, K.; Chen, Z.; Xie, G.; Liu, X.; Lin, X.; Qiu, H. J. Eight-component nanoporous high-entropy oxides with low Ru contents as high-performance bifunctional catalysts in Zn-air batteries. *Small* **2022**, *18* (12), No. 2107207.
(56) Tang, W.; He, J.; Teng, K.; Gao, L.; Qi, R.; Deng, Y.; Liu, R.; Li, A.; Fu, H.; Wang, C.-a. Toward highly efficient bifunctional electrocatalysts for zinc−air batteries: from theoretical prediction to a ternary FeCoNi design. *Nanoscale* **2022**, *14* (46), 17447−17459.
(57) Liu, K.; Huang, H.; Zhu, Y.; Wang, S.; Lyu, Z.; Han, X.; Kuang, Q.; Xie, S. Edge-segregated ternary Pd−Pt−Ni spiral nanosheets as high-performance bifunctional oxygen redox electrocatalysts for rechargeable zinc−air batteries. *J. Mater. Chem. A* **2022**, *10* (7), 3808−3817.
(58) Rui, C.; Zhang, T.; Jiang, Y.; Xie, D.; Li, M.; Lu, Q.; Bu, Y. Highly Efficient and Stable Bifunctional Electrocatalyst with Alloy/Oxide Heterostructures for a Rechargeable Zinc−Air Battery. *Energy Fuels* **2022**, *36* (20), 12816−12825.
(59) Liu, J.; Luo, Z.; Zhang, X.; Zheng, H.; Peng, L.; Qian, D.; Jia, C.; Sun-Waterhouse, D.; Waterhouse, G. I. FeCoNi nanoalloys embedded in hierarchical N-rich carbon matrix with enhanced oxygen electrocatalysis for rechargeable Zn-air batteries. *J. Mater. Chem. A* **2021**, *9* (48), 27701−27708.
(60) Yu, T.; Zhang, Y.; Hu, Y.; Hu, K.; Lin, X.; Xie, G.; Liu, X.; Reddy, K. M.; Ito, Y.; Qiu, H.-J. Twelve-component free-standing nanoporous high-entropy alloys for multifunctional electrocatalysis. *ACS Mater. Lett.* **2022**, *4* (1), 181−189.
(61) Jin, Z.; Lyu, J.; Zhao, Y.-L.; Li, H.; Chen, Z.; Lin, X.; Xie, G.; Liu, X.; Kai, J.-J.; Qiu, H.-J. Top−down synthesis of noble metal particles on high-entropy oxide supports for electrocatalysis. *Chem. Mater.* **2021**, *33* (5), 1771−1780.
(62) Wang, X.; Zhang, J.; Ma, D.; Feng, X.; Wang, L.; Wang, B. Metal−organic framework-derived trimetallic nanocomposites as efficient bifunctional oxygen catalysts for zinc−air batteries. *ACS Appl. Mater. Interfaces* **2021**, *13* (28), 33209−33217.
(63) Jin, Z.; Lyu, J.; Zhao, Y.-L.; Li, H.; Lin, X.; Xie, G.; Liu, X.; Kai, J.-J.; Qiu, H.-J. Rugged high-entropy alloy nanowires with in situ formed surface spinel oxide as highly stable electrocatalyst in Zn−air batteries. *ACS Mater. Lett.* **2020**, *2* (12), 1698−1706.
(64) Fang, G.; Gao, J.; Lv, J.; Jia, H.; Li, H.; Liu, W.; Xie, G.; Chen, Z.; Huang, Y.; Yuan, Q.; et al. Multi-component nanoporous alloy/(oxy) hydroxide for bifunctional oxygen electrocatalysis and rechargeable Zn-air batteries. *Appl. Catal., B* **2020**, *268*, No. 118431.
(65) Ramakrishnan, S.; Balamurugan, J.; Vinothkannan, M.; Kim, A. R.; Sengodan, S.; Yoo, D. J. Nitrogen-doped graphene encapsulated FeCoMoS nanoparticles as advanced trifunctional catalyst for water splitting devices and zinc−air batteries. *Appl. Catal., B* **2020**, *279*, No. 119381.
(66) Wang, Q.; Xue, Y.; Sun, S.; Yan, S.; Miao, H.; Liu, Z. Facile synthesis of ternary spinel Co−Mn−Ni nanorods as efficient bifunctional oxygen catalysts for rechargeable zinc-air batteries. *J. Power Sources* **2019**, *435*, No. 226761.
(67) Li, C.; Zhang, Z.; Wu, M.; Liu, R. FeCoNi ternary alloy embedded mesoporous carbon nanofiber: an efficient oxygen evolution catalyst for rechargeable zinc-air battery. *Mater. Lett.* **2019**, *238*, 138−142.
(68) Wang, Z.; Ang, J.; Zhang, B.; Zhang, Y.; Ma, X. Y. D.; Yan, T.; Liu, J.; Che, B.; Huang, Y.; Lu, X. FeCo/FeCoNi/N-doped carbon nanotubes grafted polyhedron-derived hybrid fibers as bifunctional oxygen electrocatalysts for durable rechargeable zinc−air battery. *Appl. Catal., B* **2019**, *254*, 26−36.
(69) Nam, G.; Son, Y.; Park, S. O.; Jeon, W. C.; Jang, H.; Park, J.; Chae, S.; Yoo, Y.; Ryu, J.; Kim, M. G. A Ternary Ni46Co40Fe14 Nanoalloy-Based Oxygen Electrocatalyst for Highly Efficient Rechargeable Zinc−Air Batteries. *Adv. Mater.* **2018**, *30* (46), No. 1803372.
(70) Lu, Y.-T.; Chien, Y.-J.; Liu, C.-F.; You, T.-H.; Hu, C.-C. Active site-engineered bifunctional electrocatalysts of ternary spinel oxides, M 0.1 Ni 0.9 Co 2 O 4 (M: Mn, Fe, Cu, Zn) for the air electrode of rechargeable zinc−air batteries. *J. Mater. Chem. A* **2017**, *5* (39), 21016−21026.
(71) Tanmathusorachai, W.; Aulia, S.; Rinawati, M.; Chang, L.-Y.; Chang, C.-Y.; Huang, W.-H.; Lin, M.-H.; Su, W.-N.; Yuliarto, B.; Yeh, M.-H. High-Entropy Prussian Blue Analogue Derived Heterostructure Nanoparticles as Bifunctional Oxygen Conversion Electrocatalysts for the Rechargeable Zinc−Air Battery. *ACS Appl. Mater. Interfaces* **2024**, *16* (45), 62022−62032.
(72) He, R.; Wang, S.; Yang, L.; Horta, S.; Ding, Y.; Di, C.; Zhang, X.; Xu, Y.; Ibáñez, M.; Zhou, Y.; et al. Active site switching on high entropy phosphides as bifunctional oxygen electrocatalysts for rechargeable/robust Zn−air battery. *Energy Environ. Sci.* **2024**, *17* (19), 7193−7208.

https://doi.org/10.1021/acs.energyfuels.5c02012
Energy Fuels 2025, 39, 13105−13119